Entropic multirelaxation lattice Boltzmann models for turbulent flows

Fabian Bösch,[*] Shyam S. Chikatamarla,[†] and Ilya V. Karlin[‡]

Department of Mechanical and Process Engineering, ETH Zurich, 8092 Zurich, Switzerland

We present three-dimensional realizations of a class of lattice Boltzmann models introduced recently by the authors [I. V. Karlin, F. Bösch, and S. S. Chikatamarla, Phys. Rev. E **90**, 031302(R) (2014)] and review the role of the entropic stabilizer. Both coarse- and fine-grid simulations are addressed for the Kida vortex flow benchmark. We show that the outstanding numerical stability and performance is independent of a particular choice of the moment representation for high-Reynolds-number flows. We report accurate results for low-order moments for homogeneous isotropic decaying turbulence and second-order grid convergence for most assessed statistical quantities. It is demonstrated that all the three-dimensional lattice Boltzmann realizations considered herein converge to the familiar lattice Bhatnagar-Gross-Krook model when the resolution is increased. Moreover, thanks to the dynamic nature of the entropic stabilizer, the present model features less compressibility effects and maintains correct energy and enstrophy dissipation. The explicit and efficient nature of the present lattice Boltzmann method renders it a promising candidate for both engineering and scientific purposes for highly turbulent flows.

I. INTRODUCTION

The lattice Boltzmann (LB) method [1,2] is a modern and highly successful kinetic-theory approach to computational fluid dynamics (CFD) and computational physics of complex flows and fluids, with applications ranging from turbulence [3] to flows at a micron scale [4] and multiphase flows [5,6], relativistic hydrodynamics [7], soft-glassy systems [8], and beyond.

While conventional CFD methods solve the Navier-Stokes equations, LB's underlying equations form a kinetic system which can be perceived as a discrete analog to Boltzmann's equation. Field variables are populations $f_i(x,t)$ corresponding to a set of discrete velocity vectors v_i, $i = 1, \ldots, b$ spanning a regularly spaced lattice with nodes x. The dynamics of populations f_i can be split into free flight (advection) and collision (relaxation) which is reflected by a general one-parametric LB equation

$$f_i(x + v_i, t + 1) = f_i' \equiv (1 - \beta) f_i(x,t) + \beta f_i^{\text{mirr}}(x,t). \quad (1)$$

Here the left-hand side is the propagation of the populations along the lattice links, while the right-hand side is the so-called postcollision state f'. The relaxation parameter β is associated with the transport coefficient of the macroscopic target equation (kinematic viscosity in the case of the incompressible Navier-Stokes equations). The mirror state f^{mirr} represents the maximally over-relaxed state. Realization of hydrodynamics in the LB setting was made possible, in the first place, with the lattice Bhatnagar-Gross-Krook (LBGK) model [9,10], in which one takes

$$f_i^{\text{mirr}} = 2 f_i^{\text{eq}} - f_i. \quad (2)$$

Here f_i^{eq} is the equilibrium which is found as a maximizer of the discrete entropy function [11,12],

$$S[f] = -\sum_{i=1}^{b} f_i \ln \left(\frac{f_i}{W_i} \right), \quad (3)$$

subject to fixed locally conserved fields identified by the first $D + 1$ velocity moments, $\rho = \sum_{i=1}^{b} f_i$ (density) and $\rho u = \sum_{i=1}^{b} v_i f_i$ (momentum density), and where the weights W_i are lattice-specific constants. With the proper symmetry of the lattice, the LBGK equation, (1) and (2), recovers the Navier-Stokes equation for the fluid velocity u, with the kinematic viscosity

$$\nu = c_s^2 \left(\frac{1}{2\beta} - \frac{1}{2} \right), \quad (4)$$

where c_s is the speed of sound [a lattice-dependent $O(1)$ constant]. The LBGK model is unambiguous since $\beta \in (0,1)$ is fixed by the kinematic viscosity (4). The limit $\beta \to 1$ (small kinematic viscosity) is particularly important as it is pertinent to achieving, if only in principle, high-Reynolds-number regimes. A notable departure from the continuous BGK approximation of Boltzmann's equation becomes manifest in the feature of over-relaxing towards the mirror state which disconnects LBGK from the kinetic theory domain $\beta \in (0, \frac{1}{2}]$ [13].

Almost immediately after its inception, the LBGK model has taken lead in the lattice Boltzmann approach to the simulation of complex hydrodynamic phenomena [2,14] and remains the "workhorse" of the LB methods to date. Popularity of LBGK is primarily based on its simplicity and outstanding computational efficiency. However, despite its promising nature and popularity, the LBGK model shows severe deficiencies (disruptive numerical instabilities) already at moderate Reynolds numbers. This precluded the LB method from making a sustainable impact in the field of computational fluid dynamics.

_____

[*]boesch@lav.mavt.ethz.ch

[†]chikatamarla@lav.mavt.ethz.ch

[‡]Corresponding author: karlin@lav.mavt.ethz.ch

A number of approaches can be found in the literature intended to alleviate this issue. We will restrict the following short discussion to methods without explicit turbulence models. Most notably, the entropic lattice Boltzmann method (ELBM) features nonlinear stability and has shown excellent performance [11,15,16]. While ELBM converges to LBGK in the resolved case, it locally alters the relaxation parameter which can be interpreted as a modification of the viscosity in order to fulfill the second law of thermodynamics by both enhancing and smoothing the features of the flow where necessary, subject to an entropy condition.

The dimension b of the kinetic space populated by f_i is usually greater than strictly necessary for recovering the Navier-Stokes equations. In three dimensions, for instance, 10 linearly independent basis vectors would suffice to represent the conserved variables and the symmetric stress tensor

$$\rho \Pi_{\alpha\beta} = \sum_{i=1}^{b} v_{i\alpha} v_{i\beta} f_i. \tag{5}$$

Although it can be shown that the coupling to the nonhydrodynamic higher moments ("ghosts") cannot be chosen arbitrarily in the limit Ma $\rightarrow 0$ [17], independent relaxation of these moments may have favorable effects on the numerical scheme's stability and accuracy.

The multiple relaxation times (MRT) LB schemes follow this line of thinking. While the relaxation of the off-diagonal parts of the stress tensor are fixed by the choice of kinematic viscosity, the MRT scheme assumes that the relaxation of higher-order moments should not affect the dynamics of the flow field (up to the Navier-Stokes level) and hence can be used to construct more stable LB schemes. Based on a separation of scales between fast and slowly varying moments a number of MRT schemes were suggested for the choice of relaxation of higher-order moments (beyond the stress tensor) [18–21].

The choice of relaxation parameters is crucial in order to increase the operational range in terms of stability and requires careful tuning. The regularized LB scheme (RLB) [22,23] was proposed to eliminate the influence of higher-order moments which may oscillate rapidly and cause numerical instabilities. In RLB, the relaxation parameters of the ghosts are chosen such as to annihilate the higher-order nonequilibrium moments in the postcollision state. As any finite lattice representation introduces discrete artifacts among the higher-order moment tensors, the regularization operation ensures isotropy, albeit in the confined subspace limited up to the stress tensor level. Although MRT and RLB models were successful in stabilizing the LB method, they still remain challenged by high Reynolds numbers [24].

Recently, we have introduced a different class of LB models without a need for tunable parameters or turbulent viscosity [25] and which demonstrates a significant extension in the operation range for simulations at high Reynolds numbers. Promising results have been reported for both two and three dimensions, as well as for complex boundaries and in presence of turbulence. Much like ELBM, entropic considerations have been employed to render the scheme stable without introducing considerable computational overhead and by keeping the simplicity and locality of the LBGK and MRT schemes. Below we shall refer to this class of models as KBC models for brevity.

In the remainder of this paper we present the construction of a family of KBC models for the standard D3Q27 lattice and review the details of the entropic stabilization. The Kida vortex flow and a randomly generated initial condition shall be employed as turbulent benchmark flows and are studied in detail for one of the realizations of KBC and the stability domain of LBGK, RLB, and KBC variations is assessed numerically.

The structure of the paper is as follows. In Sec. II, after reviewing the necessary material about the equilibrium and the moment representations for the standard lattice with $b = 27$ discrete velocities in three dimensions (D3Q27 lattice), we describe the KBC family construction. Importantly, we present a number of hydrodynamically equivalent KBC models (all the models correspond to the Navier-Stokes equation with the same kinematic (shear) viscosity) which nonetheless differ kinetically, that is, they differ by the choice of the moment representation and/or by the higher-order moments selected for the entropic stabilization. In total, eight kinetically different KBC models were considered. In Sec. IV, we first study a benchmark turbulent flow (Kida vortex flow) to demonstrate that all KBC models are unconditionally stable on coarse grids and feature the second-order grid convergence for a wide range of statistical quantities pertinent to turbulent flows. This *moment indifference* of the KBC family is contrasted to some other MRT models, particularly to the class of regularized LB in which the stability can vary significantly, depending on the choice of the moment representation. After demonstrating the moment indifference of the KBC family, one particular KBC model was used to analyze the one- and two-point statistics of the turbulent Kida vortex flow. Statistical analysis of the entropic stabilization is also provided. Finally, we report preliminary results for decaying turbulence generated by a random initial condition. Discussion in Sec. V concludes the paper.

II. THE STANDARD LATTICE IN THREE DIMENSION

A. Equilibrium

In this section, we shall remind the standard lattice in three dimensions and the corresponding equilibrium. While the material presented in this section is of a review character, we shall highlight some fundamental features of the equilibrium which were not fully discussed so far in the literature.

The standard lattice in a dimension D is built as tensor (direct) product of D copies of the fundamental one-dimensional set of discrete velocities $v_\alpha = \alpha$, where $\alpha = 0, \pm 1$:

$$v_{-1} = -1, \quad v_0 = 0, \quad v_1 = 1. \tag{6}$$

The natural D-dimensional Cartesian reference frame generated by the tensor product of D copies of the fundamental set (6) makes it convenient to enumerate the discrete velocities accordingly. Considering the three-dimensional case $D = 3$ below, we write for any of the $b = 27$ discrete velocities,

$$\boldsymbol{v}_i = (v_{ix}, v_{iy}, v_{iz}), \quad i = 1, \ldots, 27; \quad v_{i\alpha} \in \{-1, 0, 1\}. \tag{7}$$

The equilibrium on this standard D3Q27 product-lattice maximizes the entropy (3) subject to fixed conservation laws of density and momentum [12]. It is written most elegantly in

the following product-form:

$$f_i^{\text{eq}} = \rho W_i \Psi [B(u_x)]^{v_{ix}} [B(u_y)]^{v_{iy}} [B(u_z)]^{v_{iz}}, \qquad (8)$$

where the weights W_i are

$$W_i = W_{v_{ix}} W_{v_{iy}} W_{v_{iz}} \qquad (9)$$

and function Ψ is universal for all the discrete velocities (it does not depend on the discrete velocity index),

$$\Psi(\boldsymbol{u}) = A(u_x) A(u_y) A(u_z), \qquad (10)$$

with

$$A(u) = 2 - \sqrt{1 + 3u^2}. \qquad (11)$$

Furthermore, the function $B(u)$ contributing to the formation of the last term in (8) is written as

$$B(u) = \frac{2u + \sqrt{1 + 3u^2}}{1 - u}. \qquad (12)$$

Finally, the one-dimensional weights W_α in the right-hand side of (9) are dictated by the speed of sound,

$$c_s = \frac{1}{\sqrt{3}}, \qquad (13)$$

and are

$$W_0 = 2/3, \quad W_{-1} = 1/6, \quad W_1 = 1/6. \qquad (14)$$

Note that the Maxwellian in D dimensions is written as a product with respect to an arbitrarily fixed Cartesian reference frame, in accord with the familiar property of the shifted Gaussian distribution,

$$e^{-\frac{(\boldsymbol{v}-\boldsymbol{u})^2}{\theta}} = \left(\prod_{\alpha=1}^{D} e^{-\frac{v_\alpha^2}{\theta}} \right) \left(\prod_{\beta=1}^{D} e^{-\frac{u_\beta^2}{\theta}} \right) \left(\prod_{\gamma=1}^{D} \left[e^{\frac{2u_\gamma}{\sqrt{\theta}}} \right]^{\frac{v_\gamma}{\sqrt{\theta}}} \right). \quad (15)$$

It is easy to recognize the Maxwellian character of the product-lattice equilibrium (8) by comparing it to (15). The multiplication of the weights in (8) corresponds to the first multiplier in (15), the function Ψ corresponds to the second multiplier, while the product of functions B reflects the last multiplier in (15). However, the true Maxwellian is isotropic, as also revealed by reading Eq. (15) from right to left; the products collapse to a dependence on the kinetic energy in

the comoving frame alone, and the reference to the arbitrarily fixed Cartesian coordinates disappears. This is not so with the discrete velocities. It is imperative therefore to demonstrate that the product-form (8) is *manifestly isotropic* to the order of accuracy of the lattice Boltzmann model. This can be done most elegantly in the following way: Instead of expanding each population (8) into powers of the velocity components u_α, let us first expand the logarithm of f_i^{eq} (we consider a generic case of D below):

$$\ln f_i^{\text{eq}} = \ln \rho + \ln W_i + \sum_{\alpha=1}^{D} \ln A(u_\alpha) + \sum_{\alpha=1}^{D} v_{i\alpha} \ln B(u_\alpha). \qquad (16)$$

Let us denote $[\varphi(u)]_2$ the operation of the second-order truncation of the expansion of any function φ around $u = 0$ to get

$$\left[\ln f_i^{\text{eq}} \right]_2 = \ln \rho + \ln W_i - \frac{3}{2}(\boldsymbol{u} \cdot \boldsymbol{u}) + 3(\boldsymbol{v}_i \cdot \boldsymbol{u}), \qquad (17)$$

where we have used the standard notation,

$$\boldsymbol{a} \cdot \boldsymbol{b} = \sum_{\alpha=1}^{D} a_\alpha b_\alpha, \qquad (18)$$

for the Cartesian scalar product of D-dimensional vectors. Then, using the identity $[f_i^{\text{eq}}]_2 = [\exp([\ln f_i^{\text{eq}}]_2)]_2$, we get

$$\left[f_i^{\text{eq}} \right]_2 = \rho W_i \left[1 + \frac{\boldsymbol{u} \cdot \boldsymbol{v}_i}{c_s^2} + \frac{(\boldsymbol{u} \cdot \boldsymbol{v}_i)^2 - c_s^2 (\boldsymbol{u} \cdot \boldsymbol{u})}{2c_s^4} \right]. \qquad (19)$$

The second-order polynomial (19) generated by the equilibrium (8) is manifestly isotropic, and with the definition of the speed of sound $c_s = 1/\sqrt{3}$ (13) it is identical to the standard lattice Boltzmann equilibrium. Thus, both forms of the equilibrium, (8) or (19), can be used on equal footing. In the sequel, we use the exact entropic equilibrium (8).

B. Moment systems

The natural set of moments on the above D3Q27 velocity lattice is defined as

$$\rho M_{pqr} = \sum_{i=1}^{27} f_i v_{ix}^p v_{iy}^q v_{iz}^r, \quad p, q, r \in \{0, 1, 2\}. \qquad (20)$$

In the basis spanned by the natural moments, populations can be represented as

$$f_{(0,0,0)} = \rho [1 - T + M_{022} + M_{202} + M_{220} - M_{222}]$$

$$f_{(\sigma,0,0)} = \tfrac{1}{6} \rho (3\sigma u_x + 2N_{xz} - N_{yz} + T - 3\sigma Q_{xyy} - 3\sigma Q_{xzz} + 3\sigma M_{122} - 3M_{202} - 3M_{220} + 3M_{222})$$

$$f_{(0,\lambda,0)} = \tfrac{1}{6} \rho (3\lambda u_y - N_{xz} + 2N_{yz} + T - 3\lambda Q_{xxy} - 3\lambda Q_{yzz} + 3\lambda M_{212} - 3M_{022} - 3M_{220} + 3M_{222})$$

$$f_{(0,0,\delta)} = \tfrac{1}{6} \rho (3\delta u_z - N_{xz} - N_{yz} + T - 3\delta Q_{xxz} - 3\delta Q_{yyz} + 3\delta M_{221} - 3M_{022} - 3M_{202} + 3M_{222})$$

$$f_{(\sigma,\lambda,0)} = \tfrac{1}{4} \rho (\sigma\lambda \Pi_{xy} + \lambda Q_{xxy} + \sigma Q_{xyy} + M_{220} - \sigma M_{122} - \lambda M_{212} - \sigma\lambda M_{112} - M_{222})$$

$$f_{(\sigma,0,\delta)} = \tfrac{1}{4} \rho (\sigma\delta \Pi_{xz} + \delta Q_{xxz} + \sigma Q_{xzz} + M_{202} - \sigma M_{122} - \delta M_{221} - \sigma\delta M_{121} - M_{222})$$

$$f_{(0,\lambda,\delta)} = \tfrac{1}{4} \rho (\lambda\delta \Pi_{yz} + \delta Q_{yyz} + \lambda Q_{yzz} + M_{022} - \lambda M_{212} - \delta M_{221} - \lambda\delta M_{211} - M_{222})$$

$$f_{(\sigma,\lambda,\delta)} = \tfrac{1}{8} \rho (\sigma\lambda\delta Q_{xyz} + \sigma M_{122} + \lambda M_{212} + \delta M_{221} + \sigma\lambda M_{112} + \sigma\delta M_{121} + \lambda\delta M_{211} + M_{222}). \qquad (21)$$

Here we depart form the conventional single index i and use a more transparent enumeration for the discrete velocities, using indices $\sigma, \lambda, \gamma \in \{-1, 1\}$. Note that labeling of the velocities by a triad $(\cdot, \cdot, \cdot)$ is unambiguous as long as the first, the second, and the third entries are always associated with the x, the y, and the z coordinates, respectively, in the once-fixed Cartesian frame.

We chose to rename some of the natural moments as a reminder of their physical meaning:

$$T = M_{200} + M_{020} + M_{002} \tag{22}$$

is the trace of the stress tensor at unit density,

$$N_{xz} = M_{200} - M_{002}, \tag{23}$$

$$N_{yz} = M_{020} - M_{002} \tag{24}$$

are the normal stress differences at unit density, and

$$\Pi_{xy} = M_{110}, \tag{25}$$

$$\Pi_{xz} = M_{101}, \tag{26}$$

$$\Pi_{yz} = M_{011}, \tag{27}$$

are the off-diagonal components of the stress tensor at unit density. The third-order moments lack a direct physical interpretation in the isothermal case but are denoted as $Q_{xzz} = M_{102}$, $Q_{xxy} = M_{210}$, $Q_{yyz} = M_{021}$, $Q_{xxz} = M_{201}$, $Q_{yyz} = M_{021}$, and $Q_{xyz} = M_{111}$.

Another popular basis is given by the central moments of the form

$$\rho \widetilde{M}_{pqr} = \sum_{i=1}^{27} f_i (v_{ix} - u_x)^p (v_{iy} - u_y)^q (v_{iz} - u_z)^r. \tag{28}$$

Using the mapping from natural to central moments [see Appendix, Eqs. (A1)–(A23)], which is linear in the non-conserved moments, a similar moment representation of the populations in the central moments basis then can be written [(A24)–(A31)].

III. KBC FAMILY

With any of the two moment representations mentioned above (as well as for any other moment basis), we shall now review the main steps of the KBC model construction, following [25]. Let us split the contribution to each population into three parts,

$$f_i = k_i + s_i + h_i. \tag{29}$$

Here k_i (= kinematic part) depends only on the locally conserved fields. The s part s_i (= shear part) necessarily includes the (deviatoric) stress tensor

$$\mathcal{D} = \mathbf{\Pi} - \frac{1}{D} T \mathbf{I}, \tag{30}$$

where $\mathbf{I}$ is the unit tensor, and may also include further nonconserved moments (see examples below). Finally, the h part h_i (= higher-order moments) is a linear combination of the remaining higher-order moments not included in the s part.

TABLE I. Contribution of the locally conserved fields (ρ, $\mathbf{u}$), of the deviatoric stress ($\mathcal{D}$), of the trace of the stress tensor (T), and of the third-order tensor ($\mathbf{Q}$) to each of the normalized population f_i/ρ (21) of the D3Q27 lattice. Moment groups in the natural basis are listed for each discrete velocity direction.

	$\rho, \mathbf{u}$	$\mathcal{D}$	T	$\mathbf{Q}$
$(0,0,0)$	1	0	$-T$	0
$(\sigma,0,0)$	$\sigma u_x/2$	$(2N_{xz} - N_{yz})/6$	$T/6$	$-\sigma(Q_{xyy} + Q_{xzz})/2$
$(0,\lambda,0)$	$\lambda u_y/2$	$(-N_{xz} + 2N_{yz})/6$	$T/6$	$-\lambda(Q_{xxy} + Q_{yzz})/2$
$(0,0,\delta)$	$\delta u_z/2$	$(-N_{xz} - N_{yz})/6$	$T/6$	$-\delta(Q_{xxz} + Q_{yyz})/2$
$(\sigma,\lambda,0)$	0	$\sigma\lambda\Pi_{xy}/4$	0	$(\lambda Q_{xxy} + \sigma Q_{xyy})/4$
$(\sigma,0,\delta)$	0	$\sigma\delta\Pi_{xz}/4$	0	$(\delta Q_{xxz} + \sigma Q_{xzz})/4$
$(0,\lambda,\delta)$	0	$\lambda\delta\Pi_{yz}/4$	0	$(\delta Q_{yyz} + \lambda Q_{yzz})/4$
(σ,λ,δ)	0	0	0	$\sigma\lambda\delta Q_{xyz}/8$

With the representation (29), a different mirror state can be sought in a one-parameter form,

$$f_i^{\text{mirr}} = k_i + \left[2s_i^{\text{eq}} - s_i\right] + \left[(1-\gamma)h_i + \gamma h_i^{\text{eq}}\right], \tag{31}$$

where γ is a parameter which is not yet specified and the terms s_i^{eq} and h_i^{eq} denote the s and h parts evaluated at equilibrium (8). When (31) is used in (1), one arrives at nothing but a special (not the most general) MRT model. For any γ, the resulting LB model still recovers hydrodynamics with the same kinematic viscosity ν (4). For $\gamma = 2$ we obtain the LBGK model while $\gamma = 1/\beta$ results in a generalized family of "regularized" LB (RLB) models.

We shall now define several realizations of the KBC models by specifying which moments are selected for the k, s, and h parts of the populations (29). The k part includes the locally conserved moments, ρ and $\mathbf{u}$, and is the same for all realizations. Any particular model is thus fully specified by the moments retained in the s part (the h part obviously lumps all the moments not included into the k and the s parts). While including the deviatoric stress tensor $\mathcal{D}$ into the s part is mandatory for recovering the Navier-Stokes equations with the correct shear viscosity, the s part may also include other moments provided the basic symmetry properties are not violated. In particular, for the models based on the natural moment system, we consider various combinations of the deviatoric stress $\mathcal{D}$, of the trace of the stress tensor $T = \text{tr}(\mathbf{\Pi})$, and of the third-order moment $\mathbf{Q}$ to be included into the s part (see Table I for a population-wise listing).

The *kinetically* different KBC models for the natural moment representation considered below are as follows: The model KBC-N1 (where N stands for the natural moments) is characterized by the minimal choice of the s part which includes only the deviatoric stress $\mathcal{D}$. By including also the trace of the stress tensor T we get the model KBC-N2. The difference between KBC-N1 and KBC-N2 manifests through a fluctuating bulk viscosity in KBC-N1 while it is fixed in the KBC-N2 (see below). Similarly, we define the KBC-N3 model (the s part includes the deviatoric stress $\mathcal{D}$ and the third-order tensor $\mathbf{Q}$) and, finally, the KBC-N4 model (the s part includes $\mathcal{D}$, T, and $\mathbf{Q}$). Note that the kinematic k part is identical for all the four models (see Table I) and the higher-order h part is

TABLE II. Nomenclature key for the KBC models family. For each model based on the natural moment representation, KBC-N1, KBC-N2, KBC-N3, and KBC-N4, the moments constituting the s part of the populations $f_i = k_i + s_i + h_i$ are indicated. Similarly, the central moments of the s parts are indicated for the four models based on the central moments, KBC-C1, KBC-C2, KBC-C3, and KBC-C4.

Model	s Part
KBC-N1	$\mathcal{D}$
KBC-N2	$\mathcal{D}, T$
KBC-N3	$\mathcal{D}, \boldsymbol{Q}$
KBC-N4	$\mathcal{D}, T, \boldsymbol{Q}$
KNC-C1	$\tilde{\mathcal{D}}$
KBC-C2	$\tilde{\mathcal{D}}, \tilde{T}$
KBC-C3	$\tilde{\mathcal{D}}, \tilde{\boldsymbol{Q}}$
KBC-C4	$\tilde{\mathcal{D}}, \tilde{T}, \tilde{\boldsymbol{Q}}$

trivially given as

$$h_i = f_i - k_i - s_i. \tag{32}$$

Similarly, we define four KBC variations, KBC-C1, KBC-C2, KBC-C3, and KBC-C4, with respect to the central moment basis. The building blocks are now functions of the corresponding central moments and can be read off the representations given in (A24)–(A31). The nomenclature for all the models is summarized in Table II. Thus, we consider in total *eight different* KBC models, all of which give the same kinematic (shear) viscosity in the hydrodynamic limit but differ in the choice of the s part and/or in the choice of the moment representation. This extensive simulation plan is crafted in order to test the *indifference* of KBC models to a particular choice of the moment representation and/or to a particular choice of the partition into the s and h pieces.

With the standard Chapman-Enskog analysis, the above KBC models recover the density and the velocity equations in the hydrodynamic limit at low Mach number as follows:

$$\partial_t \rho = -\nabla \cdot (\rho \boldsymbol{u}), \tag{33}$$

$$\partial_t \boldsymbol{u} = -\boldsymbol{u} \cdot \nabla \boldsymbol{u} - \frac{1}{\rho} \nabla p + \frac{1}{\rho} \nabla \cdot$$
$$\times \left[\nu \rho \left(\nabla \boldsymbol{u} + \nabla \boldsymbol{u}^\dagger - \frac{2}{D} \boldsymbol{I} \nabla \cdot \boldsymbol{u} \right) \right]$$
$$+ \frac{2}{D\rho} \nabla [\xi \rho \nabla \cdot \boldsymbol{u}], \tag{34}$$

with the pressure p given by the equation of state $p = c_s^2 \rho$. For all the models, the kinematic (shear) viscosity ν is given solely by the relaxation parameter $\beta \in [0,1]$,

$$\nu = c_s^2 \left(\frac{1}{2\beta} - \frac{1}{2} \right). \tag{35}$$

The bulk viscosity differs for different realizations and is as follows:

$$\xi = \begin{cases} \nu & \text{KBC-N2, N4, C2, C4} \\ c_s^2 \left(\frac{1}{\gamma\beta} - \frac{1}{2} \right) & \text{KBC-N1, N3, C1, C3.} \end{cases} \tag{36}$$

In other words, if the trace of the stress tensor T is included into the s part of the populations, the bulk viscosity is the same as the shear viscosity (the property familiar from the LBGK and MRT models). However, if T is regarded as the higher-order moment and is included in the h part, then the bulk viscosity becomes dependent on γ. The main issue remains as to how to choose the γ.

Following Ref. [25], the major change of perspective here is that the stabilizer γ should not be considered as a free parameter, and it should not be fixed by any *ad hoc* reasoning. Rather, it has to be put under entropy control and computed by maximizing the entropy in the postcollision state f'. This matches the physics of the problem at hand, since constrained equilibria correspond to the maximum of the entropy (here the constraint is that the s part remains fixed by the over-relaxation, $s_i^{\text{mirr}} = 2s_i^{\text{eq}} - s_i$).

Specifically, let $S(\gamma)$ be the entropy of the postcollision states appearing on the right-hand side of (1), with the mirror state (31). Then we require that the stabilizer γ corresponds to maximum of this function. Introducing deviations, $\Delta s_i = s_i - s_i^{\text{eq}}$ and $\Delta h_i = h_i - h_i^{\text{eq}}$, the condition for the critical point reads:

$$\sum_{i=1}^{b} \Delta h_i \ln \left[1 + \frac{(1 - \beta\gamma)\Delta h_i - (2\beta - 1)\Delta s_i}{f_i^{\text{eq}}} \right] = 0. \tag{37}$$

Equation (37) suggests that among all nonequilibrium states with the fixed mirror values $s_i^{\text{mirr}} = 2s_i^{\text{eq}} - s_i$, we pick the one which maximizes the entropy. In contrast to MRT, the entropic stabilizer γ is not tunable but is computed at each lattice site in every time step from Eq. (37). Thus, the entropic stabilizer self-adapts to a value given by the maximum entropy condition (37). This means that the relaxation rate of the higher-order moments included into the h part depends on space and time according to the solution of (37) at each lattice node at every time steps. In particular, this leads to a local (fluctuating) bulk viscosity in the KBC models KBC-N1, KBC-N3, KBC-C1, and KBC-C3.

In order to clarify the properties of the solution to Eq. (37), let us introduce the entropic scalar product $\langle X|Y \rangle$ in the b-dimensional vector space,

$$\langle X|Y \rangle = \sum_{i=1}^{b} \frac{X_i Y_i}{f_i^{\text{eq}}}, \tag{38}$$

and expand in (37) to the first nonvanishing order in $\Delta s_i / f_i^{\text{eq}}$ and $\Delta h_i / f_i^{\text{eq}}$ to obtain

$$\gamma = \frac{1}{\beta} - \left(2 - \frac{1}{\beta} \right) \frac{\langle \Delta s | \Delta h \rangle}{\langle \Delta h | \Delta h \rangle}. \tag{39}$$

The result (39) explains the mechanism of a possible failure of the proposal $\gamma \approx 1$ at $\beta \approx 1$ (as in the regularized LB models): Whenever vectors Δs and Δh are nonorthogonal (in the sense of the entropic scalar product), the deviation of γ from $\gamma = 1$ may become very significant. Indeed, in (39), the correlation between the shear and the higher-order parts $\sim \langle \Delta s | \Delta h \rangle$ is not a correction to $\gamma = 1$ but rather a contribution of same order $O(1)$.

We found that the estimate (39) was sufficient for stabilizing all the simulations which renders the KBC an explicit and

efficient method with only slightly increased computational costs ($\sim20\%$) compared to an implementation with a fixed γ. Thus, the result (39) is key for the practical implementation of the KBC models as it defines the entropic stabilizer through explicit and compact formula instead of solving (37) numerically on each grid node at every time step.

The resulting collision operation is given here:

1	compute conserved quantities ρ, u_α
2	evaluate equilibrium $f_i^{\text{eq}}(\rho, u_\alpha)$
3	compute s and s^{eq} (see Table I)
4	compute $\Delta s_i = s_i - s_i^{\text{eq}}$
5	compute $\Delta h_i = h_i - h_i^{\text{eq}} = f_i - f_i^{\text{eq}} - \Delta s_i$
6	evaluate γ from Eq. (39)
7	relax $f_i' = f_i - \beta(2\Delta s_i + \gamma \Delta h_i)$

IV. RESULTS

A. Stability and accuracy

The Kida vortex flow is a well-studied benchmark flow which evolves from a simple deterministic and symmetric initial condition to a state which resembles a fully developed turbulent flow, which features a corresponding energy cascade. The initial conditions for the flow field are given by

$$u_x(x,y,z) = U_0 \sin x(\cos 3y \cos z - \cos y \cos 3z)$$

$$u_y(x,y,z) = U_0 \sin y(\cos 3z \cos x - \cos z \cos 3x)$$

$$u_z(x,y,z) = U_0 \sin z(\cos 3x \cos y - \cos x \cos 3y), \quad (40)$$

where $x,y,z \in [0,2\pi]$ and periodic boundary conditions are imposed in all directions. The Reynolds number is defined as $\text{Re} = U_0 N/\nu$, where N is the domain size. Initial conditions for the density (and pressure $p = \rho c_s^2$) and higher-order moments are obtained by solving the convection-diffusion equation $\frac{\partial \rho}{\partial t} + \nabla \cdot (\rho u_0) = D \triangle \rho$ on the same grid before and until steady state is reached in a similar process as described by Ref. [27].

The Kida vortex flow has been analyzed extensively using DNS [28–31]. The evolution of enstrophy shows a steep increase in the early stage of the simulation and reaches a maximum value before it decays. For the convergence study we investigate data collected from time points around the peak of enstrophy which indicates the existence of large gradients which are often numerically challenging. A simulation was considered stable if it run until the mean enstrophy,

$$\Omega = \tfrac{1}{2}\langle \boldsymbol{\omega} \cdot \boldsymbol{\omega} \rangle, \quad (41)$$

where vorticity

$$\boldsymbol{\omega} = \nabla \times \boldsymbol{u}, \quad (42)$$

was sufficiently decayed ($\Omega/\Omega_0 < 5\%$). Here $\langle \ldots \rangle$ stands for spatial averaging, and $\boldsymbol{u}'$ is the fluctuating part of the flow velocity($\langle \boldsymbol{u} \rangle = 0$ for Kida vortex),

$$\boldsymbol{u}' = \boldsymbol{u} - \langle \boldsymbol{u} \rangle. \quad (43)$$

In order to assess the stability region, the domain size $N = 100$ and initial velocity $U_0 = 0.05$ were fixed and the Reynolds number Re was increased in steps of 500. While

LBGK seized to yield sensible values at $\text{Re} \gtrsim 5000$, ELBM was always stable (tested up to $\text{Re} = 10^7$). Likewise, all the eight KBC models were always stable, independently of the moment basis or the choice of s. This outstanding stability property of all the KBC models, independent of the choice of the moment represenation and a particular choice of the s and h partition (moment indifference) has to be contrasted with the "regularized" LB (RLB) method. In the present nomenclature, the eight corresponding RLB models are obtained by fixing γ at the outset of the simulation to $\gamma = 1/\beta$. In our benchmark, only the RLB counterpart of the two KBC models, the KBC-N1 and KBC-C1, demonstrated similar stability. All other six RLB models, among them the standard RLB model [23] (the counterpart of the KBC-N2), were less stable than the LBGK model.

Computational overhead of KBC models compared to the bare LBGK method was ~ 2 times due to computation of additional moments and estimation of stabilizer γ.

Accuracy of the KBC scheme is studied in detail using Kida vortex flow at $\text{Re} = 6000$. The KBC-N4 is used as an example in all further simulations and is compared to LBGK simulation at $N = 600$ (run D) where the flow is considered to be reasonably resolved as indicated by the Kolmogorov length scale $\eta = (\nu^3/\epsilon)^{1/4} \approx 1.2$ lattice units where

$$\epsilon = \frac{1}{2}\nu \left\langle \left(\frac{\partial u_\alpha'}{\partial x_\beta} + \frac{\partial u_\beta'}{\partial x_\alpha} \right) \left(\frac{\partial u_\alpha'}{\partial x_\beta} + \frac{\partial u_\beta'}{\partial x_\alpha} \right) \right\rangle \quad (44)$$

is the dissipation rate of turbulence kinetic energy. Resolutions $N = 100, 200, 400$ are considered in the following (runs A, B, and C, respectively). Convergence towards resolved LBGK simulation is reported in Table III for various statistical quantities. Unless stated otherwise, all quantities are given in lattice units.

Figure 1 shows a comparison of the vortex structures for the four simulations roughly at the point of maximum enstrophy. The vorticity configuration is thus affected by the under-representation of large gradients in the coarse resolutions (see next section). Nevertheless, the large vortex structures are well captured at all resolutions. The largest KBC simulation (run C) is hardly distinguishable form the reference LBGK simulation (run D).

B. One-point statistics

Mean enstrophy Ω and turbulence kinetic energy

$$k = \tfrac{1}{2}\langle \boldsymbol{u}' \cdot \boldsymbol{u}' \rangle \quad (45)$$

are important global quantities characterizing the flow and its history. Figures 2 and 3, respectively, show the evolution of both quantities with nondimensional time $t = t_{\text{LB}}/(N/U_0)$. It is apparent that in the under-resolved KBC simulations $N = 100, 200$ the enstrophy peak values are not well represented. However, for coarse resolutions this is expected. The kinetic energy, on the other hand, decays quite similarly for all simulations. Table III reports the numbers at three selected time instances. During simulation, gradients are evaluated using second-order finite differences, which are solely used for reporting the enstrophy evolution in Fig. 2. All quantities based on gradients in Table III and in the remaining text and figures, however, are computed with spectral differentiation

TABLE III. Comparison of LBGK and KBC-N4 for statistical quantities in Kida vortex flow at $\text{Re} = \frac{U_0 N}{\nu} = 6000$ and $t = \frac{N}{U_0} = 0.25, 0.5, 0.75$. Resolutions $N = 100, 200, 400, 600$ for KBC runs A, B, C, and resolved LBGK run D, respectively. Convergence rate p of error with respect to LBGK solution estimated from polynomial fit (* indicates exclusion of lowest resolution). All gradient-based quantities are computed by spectral differentiation methods [26]. Turbulence characteristics: length scale $l_0 = k^{3/2}/\epsilon$, velocity scale $u_0 = k^{1/2}$, time scale $\tau_0 = l_0/u_0$, and Reynolds number $\text{Re}_0 = l_0 u_0/\nu$. Taylor characteristics: Taylor micro scale $\lambda = (15\nu u'^2/\epsilon)^{1/2}$, velocity scale $u_\lambda = u' = (2k/3)^{1/2}$ (rms turbulence intensity), time scale $\tau_\lambda = \lambda/u_\lambda$, and Reynolds number $\text{Re}_\lambda = \lambda u_\lambda/\nu$. Kolmogorov characteristics: length scale $\eta = (\nu^3/\epsilon)^{1/4}$, velocity scale $u_\eta = (\nu\epsilon)^{1/4}$, and time scale $\tau_\eta = (\nu/\epsilon)^{1/2}$.

|	$t = 0.25$					$t = 0.5$					$t = 0.75$				
	A	B	C	**D**	p	A	B	C	**D**	p	A	B	C	**D**	p
$k \times 10^4$	8.528	8.644	8.663	**8.657**	2.25	6.237	6.385	6.411	**6.402**	2.06	3.808	3.947	3.965	**3.954**	1.87
$\Omega \times N^2$	1.479	1.736	1.784	**1.784**	7.00	1.954	2.796	3.174	**3.216**	2.46	1.581	2.137	2.262	**2.301**	2.12
$\epsilon \times 10^5 N$	2.473	2.893	2.974	**2.974**	5.17	3.333	4.665	5.290	**5.360**	2.43	2.730	3.566	3.771	**3.835**	2.06
$S3 \times 10^2$	10.66	7.427	9.076	**10.34**	1.21*	28.88	39.06	47.82	**48.98**	2.05	28.57	33.96	39.73	**39.99**	2.72
$S4$	5.082	6.200	6.176	**6.149**	2.64	4.019	5.237	6.067	**6.160**	2.26	4.149	4.326	4.842	**4.843**	4.81
$S5$	2.863	2.194	2.475	**2.892**	0.744*	3.216	6.130	9.062	**9.696**	1.68	4.320	4.347	6.081	**5.980**	2.02
$S6$	52.63	84.47	81.22	**79.34**	1.91	34.77	67.61	97.02	**100.1**	2.20	39.48	36.43	51.77	**51.56**	2.95
$l_0 \times 10^1/N$	10.07	8.784	8.573	**8.564**	3.65	4.674	3.459	3.069	**3.022**	2.57	2.722	2.199	2.093	**2.050**	1.98
$u_0 \times 10^2$	2.920	2.940	2.943	**2.942**	2.26	2.497	2.527	2.532	**2.530**	2.06	1.951	1.987	1.991	**1.988**	1.88
τ_0/N	34.49	29.88	29.13	**29.11**	3.94	18.71	13.69	12.12	**11.94**	2.63	13.95	11.07	10.51	**10.31**	2.08
Re_0	3530	3099	3028	**3024**	3.43	1401	1049	932.4	**917.5**	2.51	637.4	524.2	500.2	**489.2**	1.87
$\lambda \times 10^2/N$	5.361	4.990	4.927	**4.925**	3.91	3.949	3.378	3.178	**3.155**	2.55	3.409	3.037	2.960	**2.931**	2.03
$u_\lambda \times 10^2$	2.384	2.400	2.403	**2.402**	2.26	2.039	2.063	2.067	**2.066**	2.06	1.593	1.622	1.626	**1.624**	1.88
τ_λ/N	2.248	2.079	2.050	**2.050**	5.27	1.937	1.637	1.537	**1.527**	2.67	2.140	1.872	1.821	**1.805**	2.23
Re_λ	153.4	143.7	142.1	**142.0**	3.40	96.63	83.62	78.84	**78.21**	2.43	65.19	59.12	57.75	**57.11**	1.83
$\eta \times 10^3/N$	2.200	2.115	2.100	**2.100**	5.26	2.041	1.877	1.819	**1.813**	2.63	2.146	2.007	1.979	**1.971**	2.20
$u_\eta \times 10^3$	3.789	3.940	3.968	**3.968**	5.22	4.082	4.440	4.582	**4.597**	2.55	3.884	4.152	4.210	**4.228**	2.14
$\tau_\eta \times 10^1/N$	5.805	5.367	5.293	**5.293**	5.27	5.000	4.227	3.969	**3.943**	2.67	5.525	4.834	4.701	**4.662**	2.23
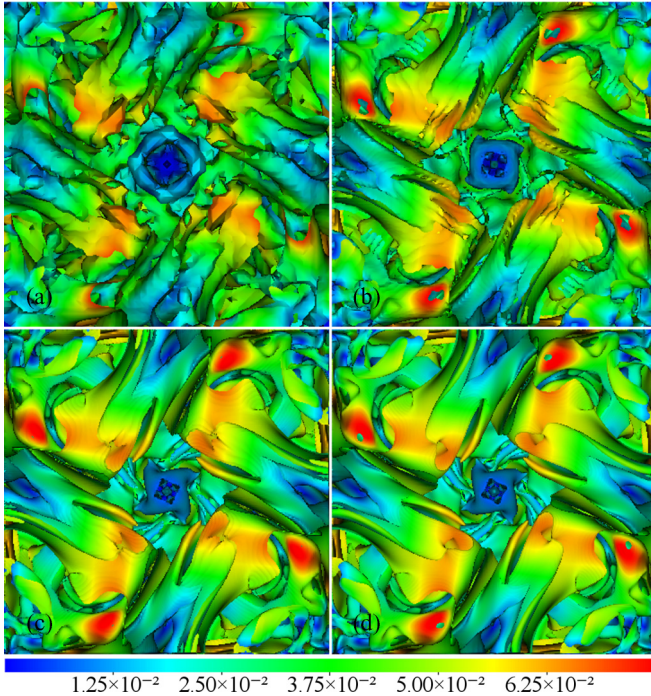
FIG. 1. (Color online) Isosurface of vorticity component $\omega_z = 0$ at time $t = 0.5$ colored with velocity magnitude rendered at $z = 0$, $x, y \in [0, \pi]$ plane. Runs A ($N = 100$), B ($N = 200$), C ($N = 400$), and D ($N = 600$, reference solution).

methods [26], unless stated otherwise. This also explains the discrepancies in enstrophy between Fig. 2 and Table III for the lowest resolution $N = 100$.

While the energy seems to be dissipated similarly with time it is important to study the kinetic energy k and dissipation rate ϵ thereof across flow scales in order to decide whether low-order statistics of turbulent flows yield sensible values in coarse resolution simulations despite the under-representation of high gradients. The instrument at hand is the spectral representation of the kinetic energy distribution $E(\kappa)$, where $\kappa = |\boldsymbol{\kappa}|$ is the modulus of the wave number vector. Figure 4 shows the
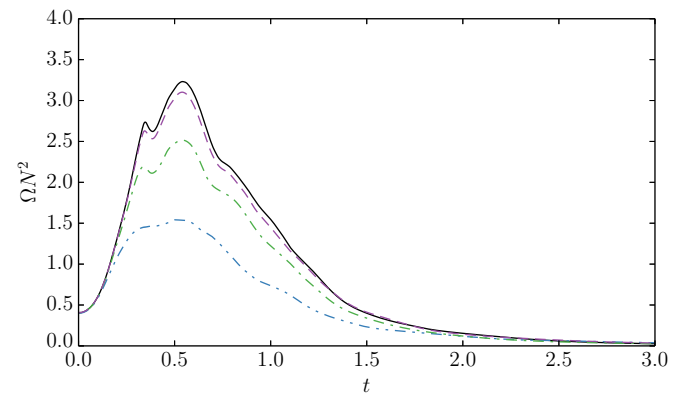

FIG. 2. (Color online) Mean enstrophy evolution with time for simulations A ($- \cdot \cdot$), B ($- \cdot$), C ($- -$), and D ($-$). Gradients evaluated with second order of accuracy.
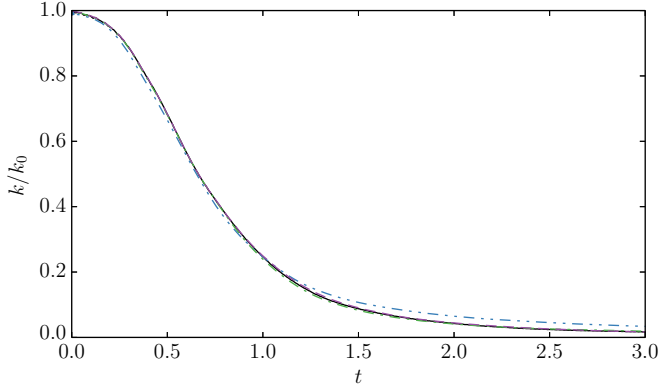
FIG. 3. (Color online) Kinetic energy evolution with time for simulations A $(- \cdot \cdot)$, B $(- \cdot)$, C $(--)$, and D $(-)$.

nondimensional energy density distribution normalized with kinetic energy,

$$k = \int_0^\infty E(\kappa) \, d\kappa. \tag{46}$$

According to Refs. [32,33], the energy scales as $E \sim \kappa^{-5/3}$ in the inertial subrange. The studied Kida flow here does not exhibit large-enough Reynolds numbers to see an extended inertial range. However, it is apparent that the energy scales similarly across resolutions and a sharp cutoff is visible at the smallest scales. This indicates that the KBC model is capable of producing the expected energy distribution throughout the scales without an explicit turbulence model. A case for higher Reynolds number shall be examined below.

The cumulative distribution function of the energy-dissipation rate density

$$D(\kappa) = 2\nu\kappa^2 E(\kappa) \tag{47}$$

illustrates the scales of eddies responsible for the dissipation process, see Fig. 5. The under-resolved simulations employ expectedly larger eddies for the bulk of the dissipation [see also Table III where the energy dissipation rate $\epsilon = \int_0^\infty D(\kappa) \, d\kappa$ is reported].
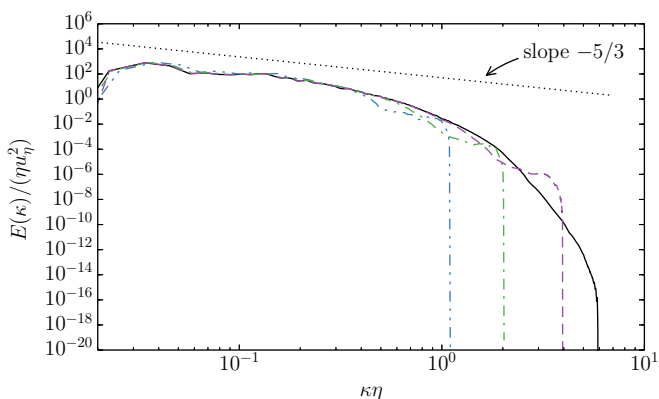

FIG. 4. (Color online) Kinetic energy density spectrum at $t = 0.5$ for simulations A $(- \cdot \cdot)$, B $(- \cdot)$, C $(--)$, and D $(-)$. The dotted line with slope $-5/3$ shows the Kolmogorov scaling.
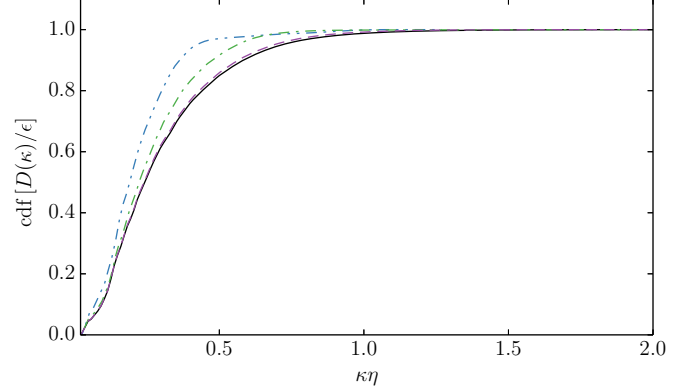

FIG. 5. (Color online) Cumulative distribution function of the energy-dissipation rate density $D(\kappa)$ at time $t = 0.5$ for simulations A $(- \cdot \cdot)$, B $(- \cdot)$, C $(--)$, and D $(-)$.

The longitudinal skewness factor

$$S_{11}^n = (-1)^n \left\langle \left(\frac{\partial u'_x}{\partial x} \right)^n \right\rangle \left\langle \left(\frac{\partial u'_x}{\partial x} \right)^2 \right\rangle^{-n/2} \tag{48}$$

is another global statistical quantity in real space which we report in Table III. In agreement with Fig. 2 we find that the outcome of the lowest resolution $N = 100$ is rather inconsistent with the trend observed in the other simulations; however, it agrees well with the resolved case. The lower convergence rate for the odd-order skewness factors may be caused by the inherent lack of isotropy in the third-order moments. However, further studies are needed to draw a concise conclusion.

The remainder of Table III is a compilation of the turbulence, Taylor, and Kolmogorov flow scales. Here and with the vast majority of the reported quantities we observe a second-order grid convergence rate, as expected in the context of LB simulations.

C. Two-point statistics

The longitudinal structure function of order n defined as

$$B_{11}^n = (-1)^n \left\langle \left(\frac{\partial u'_x}{\partial x} \right)^n \right\rangle \left\langle \left(\frac{\partial u'_x}{\partial x} \right)^2 \right\rangle^{-n/2} \tag{49}$$

exhibits linear scaling on logarithmic plots [32,33]. In particular, the second-order structure function scales as $B_{11}^2 \sim r^{2/3}$. Figure 6 depicts the results with the theoretical scaling. Due to the relatively low Reynolds number we may not identify an extended inertial range but we note that the simulations agree well with the reference over the entire range of r.

Another real-space two-point statistical quantity that can be used to assess different numerical techniques is the correlation of the velocity field. Here the longitudinal and transverse correlation functions are defined as

$$\rho_{11}^n(r) = \frac{\langle u'_x(x,y,z) u'_x(x+r,y,z) \rangle}{\langle u'_x(x,y,z) u'_x(x,y,z) \rangle}, \tag{50}$$

$$\rho_{22}^n(r) = \frac{\langle u'_y(x,y,z) u'_y(x+r,y,z) \rangle}{\langle u'_y(x,y,z) u'_y(x,y,z) \rangle}. \tag{51}$$
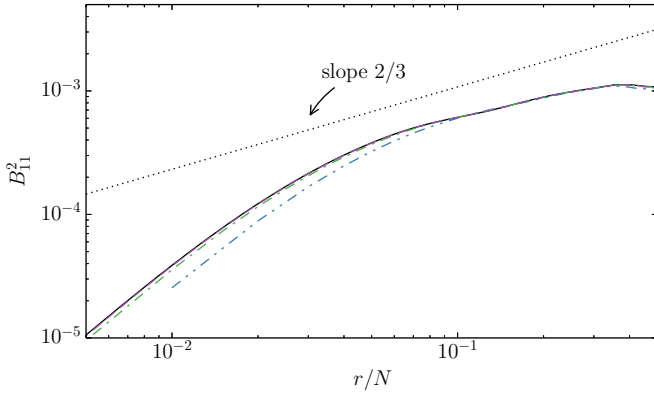
FIG. 6. (Color online) Second order longitudinal structure function at $t = 0.5$ for simulations A $(- \cdot \cdot)$, B $(- \cdot)$, C $(- -)$, and D $(-)$. The dotted line indicates the theoretical scaling.

A comparison at time $t = 0.5$ is given in Fig. 7. All simulations with $N \geqslant 200$ show excellent agreement with the reference solution. At the maximum distance $r = 0.5$ the velocity components are still correlated, which is associated with the low Reynolds number (see Fig. 12 for comparison).

D. Stabilizer γ and the LBGK limit

The importance of the self-adjusting stabilizer γ becomes clear when considering its evolution in time and its distribution in space. In fact, the evolution of γ is closely correlated with the flow field (see Fig. 8). In the regions of higher turbulence intensity it is distinctly different in the mean and shows larger fluctuations. Figure 8 depicts the spatial variation of γ for the simulations A, B, and C. For the run A (the coarsest resolution) the variations of the stabilizer are large but diminish subsequently when resolution is increased. Note that for $N = 400$ a large part of the domain governed by $\gamma \sim 2$ (green areas). The distribution of γ in space reveals the close relation of γ to the flow, as can be seen by the superimposed vorticity magnitude contours in Fig. 8.

In general, we observe that when the spatial resolution is increased the mean of stabilizer tends to the value $\gamma = 2$ and shows significantly smaller fluctuations. For the discussion in
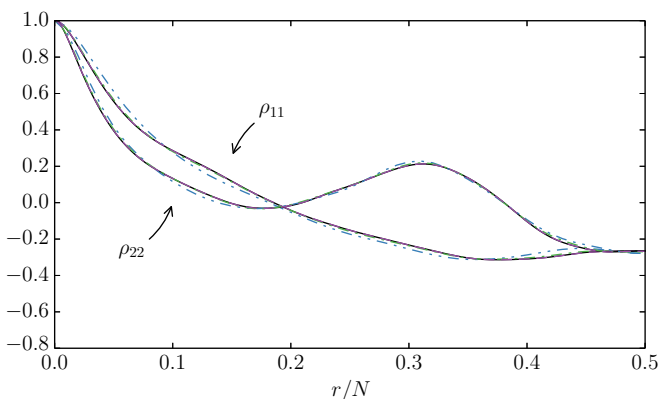

FIG. 7. (Color online) Longitudinal and transverse velocity correlation functions at $t = 0.5$ for simulations A $(- \cdot \cdot)$, B $(- \cdot)$, C $(- -)$, and D $(-)$.

this and the next sections, we executed a control run (run E hereafter) on the grid $N = 600$ with the selected KBC-N4 model, that is, with the same resolution as for the LBGK simulation of the run D. Figure 9 shows the mean stabilizer $\langle \gamma \rangle$ at $N = 100$ and $N = 600$ (runs A and E, respectively), together with its standard deviation. It is apparent that $\langle \gamma \rangle$ is far form being constant in the low-resolution case, whereas $\langle \gamma \rangle = 2$ and fluctuations around the mean value are tight (but not negligible) for the highest resolution (run E). This gives yet another indication of convergence towards the LBGK model which has a fixed value of $\gamma = 2$. It is remarkable that the LBGK limit $\gamma = 2$ is found for all the eight KBC models in this and other three-dimensional simulations (this is at variance with the two-dimensional case, see Ref. [34]). While we defer analytical proof of this statement based on Eq. (39) to a separate study, it is important to observe that the KBC models automatically tend to the LBGK limit once the resolution is increased. This feature (achieving the LBGK limit) of the KBC models is similar to the known property of the standard entropic LB (ELBM) and is different from any MRT model with *a priori* fixed relaxation times.

E. Convergence to the Navier-Stokes equation at small scales

In the previous sections convergence of KBC models towards LBGK was demonstrated through various low-order statistical quantities, as well as by the analysis of the stabilizer. Table IV shows the relative difference of selected statistical quantities between the two reasonably resolved simulations on the grid of same size $N = 600$, run D (LBGK) and run E (KBC-N4). The majority of the quantities are within a margin of 0.5% throughout the range of time (around the peak turbulence intensity). This shows that the two models produce almost identical results at sufficiently large resolutions.

A slightly larger difference ($\sim$1%) is reported for the mean enstrophy Ω and the dissipation rate ϵ which are directly dependent on the gradients in the system. The origin of these differences may be explained by considering compliance with the constraint of incompressibility, $\nabla \cdot \boldsymbol{u} = 0$. As the lattice Boltzmann method is weakly compressible, i.e., the pressure field is imposed by equation of state and not by solving the pressure-Poisson equation, this is of general interest regarding the quality of a simulation. Figure 10 shows the root mean square of the divergence of the velocity for the runs D and E. It is apparent that the LBGK model leads to a slightly larger compressibility as compared to the KBC on the grid of same size. This can be attributed to the fluctuations of the stabilizer γ in the KBC model which still persist even when the mean has reached the LBGK value $\langle \gamma \rangle = 2$ (see Fig. 9). Note that the mean of the divergence, $\langle \nabla \cdot \boldsymbol{u} \rangle$, vanishes for all the models. It is also noted that KBC models which allow for a fluctuating bulk viscosity are even less compressible than both LBGK and the KBC models with the fixed bulk viscosity, especially for low resolution.

While the energy cascade and the evolution of the low-order statistics show the trends which one would expect from a realization of the incompressible flow, it is still of interest to quantify the recovery of the Navier-Stokes equations at small scales. To that end, let us remind that the incompressible Navier-Stokes equation implies the following balance
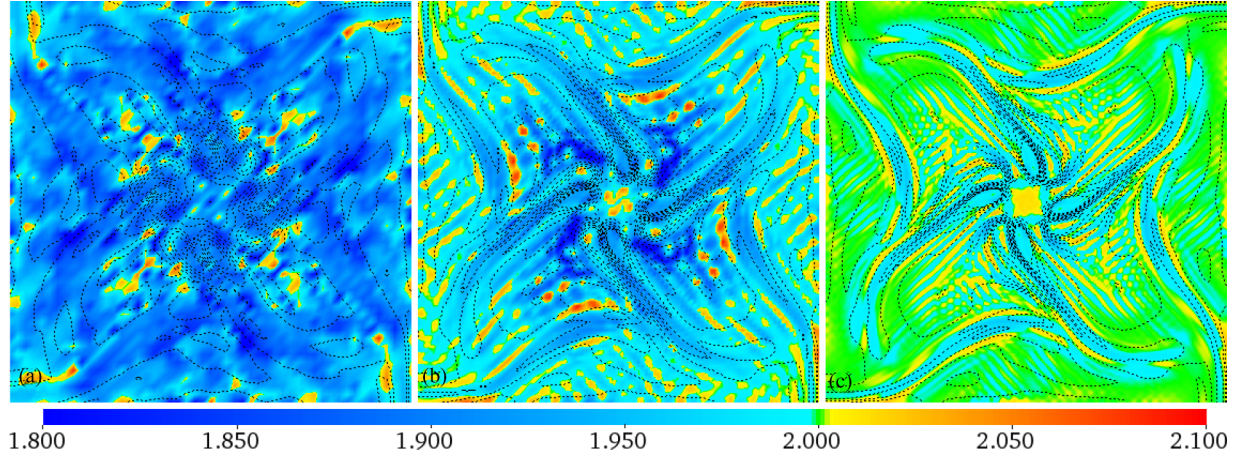
FIG. 8. (Color online) Snapshot of the stabilizer γ (color field) with superimposed contours of vorticity magnitude (dashed curves) for simulations A, B, and C on the plane $z = 1.068$ and $x,y \in [0,\pi]$ (only one quarter of the domain is shown due to symmetry) at $t = 0.25$.

equations for the averaged momentum, vorticity, energy, and enstrophy which yield for statistically homogeneous flows [35,36],

$$\partial_t \langle \boldsymbol{u} \rangle = 0, \tag{52}$$

$$\partial_t \langle \boldsymbol{\omega} \rangle = 0, \tag{53}$$

$$\partial_t k = -2\nu\Omega, \tag{54}$$

$$\partial_t \Omega = \langle \boldsymbol{\omega} \cdot \boldsymbol{s} \cdot \boldsymbol{\omega} \rangle - 2\nu P, \tag{55}$$

where

$$\boldsymbol{s} = \tfrac{1}{2}(\nabla \boldsymbol{u} + \nabla \boldsymbol{u}^{\dagger}), \tag{56}$$

is the rate-of-strain tensor, and P is the palinstrophy,

$$P = \tfrac{1}{2}\langle \nabla \boldsymbol{\omega} : \nabla \boldsymbol{\omega} \rangle. \tag{57}$$

While the global conservation of average momentum (52) and vorticity (53) are satisfied up to machine precision for all times and all resolutions considered above, the balance of various terms in the energy (54) and enstrophy (55) equations is directly probing the recovery of the Navier-Stokes equation

at small scales by the KBC model. To that end, we recast the balance equations (54) and (55) in terms of the effective viscosity,

$$\nu_{\text{eff},k} = -\frac{\partial_t k}{2\Omega}, \tag{58}$$

$$\nu_{\text{eff},\Omega} = \frac{\langle \boldsymbol{\omega} \cdot \boldsymbol{s} \cdot \boldsymbol{\omega} \rangle - \partial_t \Omega}{2P}. \tag{59}$$

In the simulation, the Navier-Stokes equation will be verified at small scales if the ratio $\nu_{\text{eff}}/\nu \approx 1$. Thus, evaluation of effective viscosities (58) and (59) is an important check of the accuracy, which is also used in the standard CFD methods.

Equations (52), (53), (58), and (59) are evaluated for simulations A, B, C, and E where the time and space derivatives are computed with fourth-order accurate central differences and spectral differentiation, respectively. The effective viscosity ratio based on the energy balance (58) is reported in Table V. By increasing the resolution the values are approaching $\nu_{\text{eff},k}/\nu \approx 1$. It is apparent that even for the coarsest run A the additional dissipation is rather small, which is consistent with the evolution of turbulence kinetic energy k shown in Fig. 3. Note that at the highest resolution, the effective viscosity fluctuates around the target value ν, with *lower* values (that is, with a higher effective Reynolds number). The second effective viscosity $\nu_{\text{eff},\Omega}$, reported in Table VI, is considerably larger for
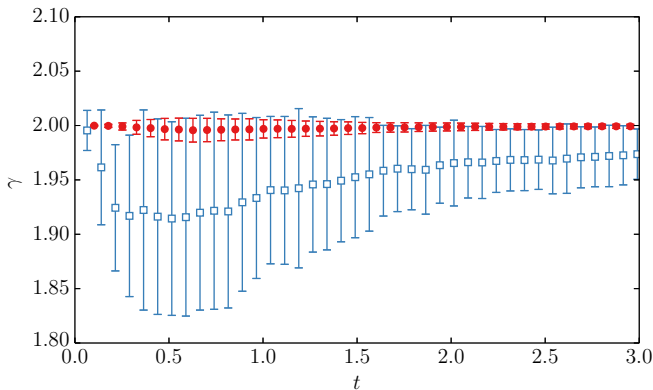

FIG. 9. (Color online) Evolution of the mean entropic stabilizer γ (symbols) and its standard deviation (error bars) with time for simulation A (open symbols) and E (full symbols).

TABLE IV. Relative difference in percentage of statistical quantities in Kida vortex flow at $\text{Re} = \frac{U_0 N}{\nu} = 6000$ for times $t = \frac{N}{U_0} = 0.25, 0.5, 0.75, 1.0$ and resolution $N = 600$ for LBGK (run D) and KBC (run E).

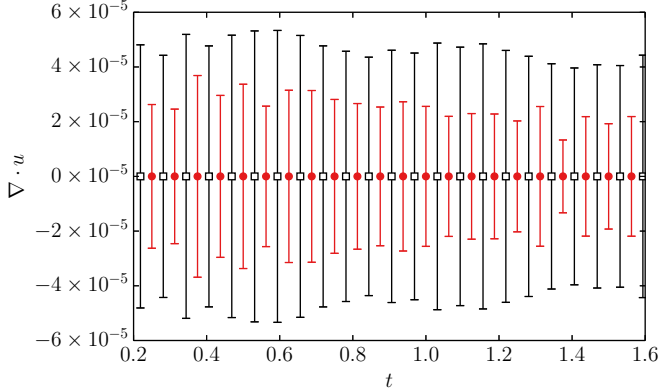| Time	0.25	0.5	0.75	1.0
k	0.09672	0.1957	0.1581	0.5773
u'	0.04835	0.09782	0.07901	0.2891
Ω	0.2747	0.4154	1.009	0.9649
ϵ	0.2663	0.4166	1.006	0.9674
λ	0.08461	0.1100	0.4206	0.1967
Re_λ	0.0363	0.01232	0.342	0.09292
η	0.06647	0.1039	0.2499	0.2433

FIG. 10. (Color online) Mean (symbols) and rms fluctuations (error bars) of the compressibility $\nabla \cdot \boldsymbol{u}$ for runs D (LBGK, open symbols) and E (KBC-N4, full symbols) with time. Gradients evaluated with second order of accuracy.

simulations A and B, which is expected from comparison to the mean enstrophy dynamics shown in Fig. 2. However, for larger resolutions the values are close to the nominal viscosity.

Thus, we conclude that the KBC scheme recovers well the Navier-Stokes equations for reasonable resolutions while introducing only small additional dissipation at coarse grid simulations. We also note that we have not found a consistency check as above done on other available LB models in the literature.

F. Large Reynolds numbers

The second numerical example considered in this paper is the simulation of a highly turbulent flow starting from a random initial condition and decaying with time. The periodic and cubic domain with box length $N = 400$ was initialized with a flow field generated from a prescribed narrow-banded initial energy spectrum peaked at grid wave number $\frac{\kappa_0 N}{2\pi} \approx 8$,

$$E_0 = 400 \left(\frac{2}{3}\right)^{1/4} \left(2 \nu u_0'^3/\pi\right)^{1/2} b^2 \kappa^4 \exp\left[-b\kappa^2\right],$$
$$(60)$$
$$b = 20000 \left(\frac{2}{3}\right)^{1/2} \nu/u_0',$$

where $\nu = 8.164970 \times 10^{-5}$ and $u_0' = 0.01$. The initial values of the density (and pressure) and the higher-order moments were generated with the same procedure as described earlier for the Kida flow.

The main objective is to test the KBC scheme for an under-resolved simulation (Kolmogorov scale $\eta \approx 10$ lattice

TABLE V. Effective viscosity ratio $\nu_{\mathrm{eff},k}/\nu$ for simulations A, B, C, and E at different time instances.

Time	0.25	0.5	0.75	1.0
Run A	1.5971	1.5210	1.5640	1.4698
Run B	1.1173	1.1507	1.1356	1.0595
Run C	1.0303	1.0311	1.0030	0.9302
Run E	0.9875	1.0039	0.9976	0.9005

TABLE VI. Effective viscosity ratio $\nu_{\mathrm{eff},\Omega}/\nu$ for simulations A, B, C, and E at different time instances.

Time	0.25	0.5	0.75	1.0
Run A	2.2622	2.2577	2.0950	1.8545
Run B	1.2603	1.4505	1.4042	1.3943
Run C	1.0575	1.1120	1.0912	1.0776
Run E	1.0282	1.0474	1.0337	1.0383

units) at large Reynolds numbers (Re$_\lambda \approx 600$). In particular, we ask whether the scheme is stable for a random and highly turbulent flow in absence of a deterministic and highly symmetric initial condition, whether low-order statistics are well represented and physical dissipation (i.e., scaling laws) is modeled correctly. By means of this simulation we examine the general question of the performance for large Reynolds numbers in an under-resolved simulation from yet another point of view. While a resolved simulation was not attempted, we compare our results to the classical scaling laws.

Figure 11 shows the turbulence kinetic energy spectrum at $t = t_{\mathrm{LB}}/(N/u_0') = 0.075$. The inertial range is extended and the scaling is more apparent than in the less turbulent simulations above. The sharp cutoff at the smallest scales is still maintained despite the coarse resolution. As before, numerical stability is naturally guaranteed to very high Reynolds numbers. While the initial spectrum is narrow and steep, it flattens during the course of energy decay and exhibits the Kolmogorov scaling in the inertial subrange roughly at the peak of mean enstrophy. Figure 12 shows the velocity correlations where the contributions to the correlations are vanishing for $r/N > 0.2$ at $t = 0.075$. Hence, the velocity field is largely uncorrelated as one would expect from isotropic homogeneous turbulent flows. While these results are far from a comprehensive study, they contribute to the overall assessment that the KBC scheme might perform well even in the case of severe under-resolution. A more comprehensive investigation shall be conducted in a further study.
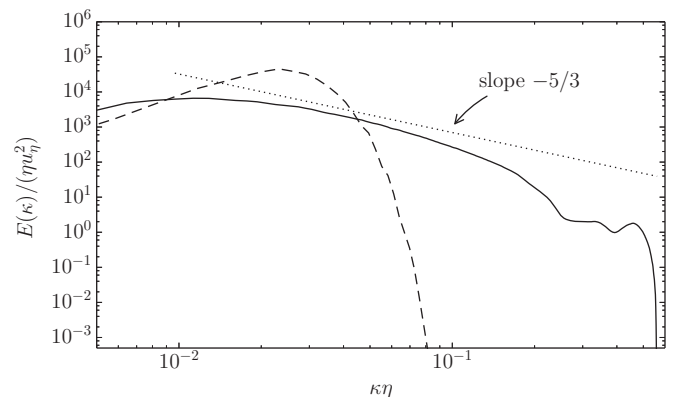

FIG. 11. Turbulence kinetic energy spectrum at Re$_\lambda = 564$, $t = 0.075$ (solid) and initial spectrum at Re$_\lambda = 2000$ (dashed). The dotted line indicates the theoretical scaling.
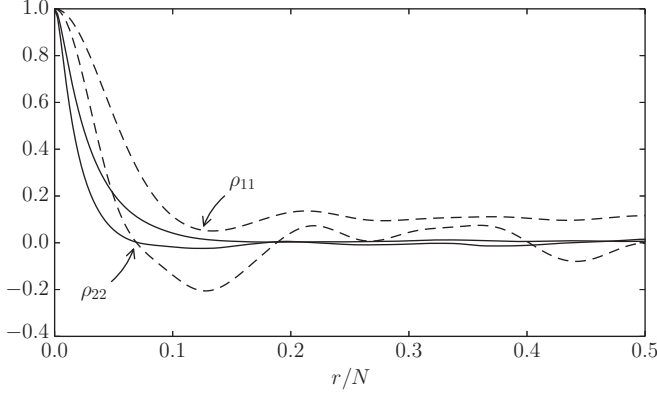
FIG. 12. Longitudinal and transversal velocity correlation functions at $\mathrm{Re}_\lambda = 564, t = 0.075$ (solid) and initial values at $\mathrm{Re}_\lambda = 2000$ (dashed).

V. CONCLUSIONS

We presented the three-dimensional realizations of the KBC class of lattice Boltzmann models for the D3Q27 lattice. We reviewed the details of the entropic stabilization and described eight variations of the KBC scheme. Stability and accuracy was studied in detail for homogeneous isotropic turbulence. A detailed comparison with LBGK was carried out at various grid resolutions. Second-order rate of convergence was numerically confirmed in the vast majority of the statistical quantities of interest. It must be stressed that the entropic KBC models were found stable (in contrast to LBGK and RLB) for all the considered cases here, despite under-resolution and high Reynolds numbers. This demonstrates that the KBC approach is moment indifferent, unlike other versions of MRT models.

The KBC models were shown to capture the expected scaling law for energy spectra in the case of high Reynolds numbers. Low-order statistics such as averages of kinetic energy, enstrophy, and rate of dissipation as well as the spectral densities for energy and rate of dissipation agree well with resolved simulation despite the under-resolution.

In general, we showed that by keeping the kinematic (shear) viscosity coefficient constant the presented method is stable numerically and produces accurate results in the presence of under-resolution. These findings and the parameter-free and explicit nature of KBC as well as the lack of explicit turbulence modeling renders the scheme a promising candidate for applications in both research and engineering contexts where high Reynolds numbers and computational cost are of importance.

It has been demonstrated in Ref. [25] that also for three-dimensional flows in the presence of complex walls, low-order statistics can be captured well using KBC. In a further publication we will address the issue of boundary conditions for KBC models in both two and three dimensions.

APPENDIX: CENTRAL MOMENTS

The mapping between natural and central moments is linear in the nonconserved moments and given by the following relations:

$$\widetilde{\Pi}_{xy} = \Pi_{xy} - u_x u_y, \tag{A1}$$

$$\widetilde{\Pi}_{xz} = \Pi_{xz} - u_x u_z, \tag{A2}$$

$$\widetilde{\Pi}_{yz} = \Pi_{yz} - u_y u_z, \tag{A3}$$

$$\widetilde{N}_{xz} = N_{xz} - u_x^2 + u_z^2, \tag{A4}$$

$$\widetilde{N}_{yz} = N_{yz} - u_y^2 + u_z^2, \tag{A5}$$

$$\widetilde{T} = T - (u_x^2 + u_y^2 + u_z^2), \tag{A6}$$

$$\widetilde{Q}_{xyz} = Q_{xyz} - u_x \widetilde{\Pi}_{yz} - u_y \widetilde{\Pi}_{xz} - u_z \widetilde{\Pi}_{xy} - u_x u_y u_z, \tag{A7}$$

$$\widetilde{Q}_{xyy} = Q_{xyy} - \tfrac{1}{3}\big[6u_y \widetilde{\Pi}_{xy} + u_x(3u_y^2 + 2\widetilde{N}_{yz} - \widetilde{N}_{xz} + \widetilde{T})\big], \tag{A8}$$

$$\widetilde{Q}_{xzz} = Q_{xzz} - \tfrac{1}{3}\big[6u_z \widetilde{\Pi}_{xz} + u_x(3u_z^2 - \widetilde{N}_{xz} - \widetilde{N}_{yz} + \widetilde{T})\big], \tag{A9}$$

$$\widetilde{Q}_{xxy} = Q_{xxy} - \tfrac{1}{3}\big[6u_x \widetilde{\Pi}_{xy} + u_y(3u_x^2 + 2\widetilde{N}_{xz} - \widetilde{N}_{yz} + \widetilde{T})\big], \tag{A10}$$

$$\widetilde{Q}_{yzz} = Q_{yzz} - \tfrac{1}{3}\big[6u_z \widetilde{\Pi}_{yz} + u_y(3u_z^2 - \widetilde{N}_{xz} - \widetilde{N}_{yz} + \widetilde{T})\big], \tag{A11}$$

$$\widetilde{Q}_{xxz} = Q_{xxz} - \tfrac{1}{3}\big[6u_x \widetilde{\Pi}_{xz} + u_z(3u_x^2 + 2\widetilde{N}_{xz} - \widetilde{N}_{yz} + \widetilde{T})\big], \tag{A12}$$

$$\widetilde{Q}_{yyz} = Q_{yyz} - \tfrac{1}{3}\big[6u_y \widetilde{\Pi}_{yz} + u_z(3u_y^2 + 2\widetilde{N}_{yz} - \widetilde{N}_{xz} + \widetilde{T})\big], \tag{A13}$$

$$\widetilde{M}_{022} = M_{022} - \left[u_y^2 u_z^2 + 4u_y u_z \widetilde{\Pi}_{yz} + \left(u_y^2 + u_z^2 \right) \widetilde{T}/3 - \left(u_y^2 + u_z^2 \right) \widetilde{N}_{xz}/3 + \left(-u_y^2 + 2u_z^2 \right) \widetilde{N}_{yz}/3 + 2u_y \widetilde{Q}_{yzz} + 2u_z \widetilde{Q}_{yyz} \right],$$

(A14)

$$\widetilde{M}_{202} = M_{202} - \left[u_x^2 u_z^2 + 4u_x u_z \widetilde{\Pi}_{xz} + \left(u_x^2 + u_z^2 \right) \widetilde{T}/3 + \left(-u_x^2 + 2u_z^2 \right) \widetilde{N}_{xz}/3 - \left(u_x^2 + u_z^2 \right) \widetilde{N}_{yz}/3 + 2u_x \widetilde{Q}_{xzz} + 2u_z \widetilde{Q}_{xxz} \right],$$

(A15)

$$\widetilde{M}_{220} = M_{220} - \left[u_x^2 u_y^2 + 4u_x u_y \widetilde{\Pi}_{xy} + \left(u_x^2 + u_y^2 \right) \widetilde{T}/3 + \left(-u_x^2 + 2u_y^2 \right) \widetilde{N}_{xz}/3 + \left(2u_x^2 - u_y^2 \right) \widetilde{N}_{yz}/3 + 2u_x \widetilde{Q}_{xyy} + 2u_y \widetilde{Q}_{xxy} \right]$$

(A16)

$$\widetilde{M}_{211} = M_{211} - \left(u_x^2 u_y u_z + 2u_x u_z \widetilde{\Pi}_{xy} + 2u_x u_y \widetilde{\Pi}_{xz} + u_x^2 \widetilde{\Pi}_{yz} + u_y u_z \widetilde{T}/3 + 2u_y u_z \widetilde{N}_{xz}/3 \right.$$
$$\left. - u_y u_z \widetilde{N}_{yz}/3 + 2u_x \widetilde{Q}_{xyz} + u_z \widetilde{Q}_{xxy} + u_y \widetilde{Q}_{xxz} \right),$$

(A17)

$$\widetilde{M}_{121} = M_{121} - \left(u_x u_y^2 u_z + 2u_y u_z \widetilde{\Pi}_{xy} + u_y^2 \widetilde{\Pi}_{xz} + 2u_x u_y \widetilde{\Pi}_{yz} + u_x u_z \widetilde{T}/3 - u_x u_z \widetilde{N}_{xz}/3 + 2u_x u_z \widetilde{N}_{yz}/3 \right.$$
$$\left. + 2u_y \widetilde{Q}_{xyz} + u_z \widetilde{Q}_{xyy} + u_x \widetilde{Q}_{yyz} \right),$$

(A18)

$$\widetilde{M}_{112} = M_{112} - \left(u_x u_y u_z^2 + u_z^2 \widetilde{\Pi}_{xy} + 2u_y u_z \widetilde{\Pi}_{xz} + 2u_x u_z \widetilde{\Pi}_{yz} + u_x u_y \widetilde{T}/3 - u_x u_y \widetilde{N}_{xz}/3 \right.$$
$$\left. - u_x u_y \widetilde{N}_{yz}/3 + 2u_z \widetilde{Q}_{xyz} + u_y \widetilde{Q}_{xzz} + u_x \widetilde{Q}_{yzz} \right),$$

(A19)

$$\widetilde{M}_{122} = M_{122} - \left[u_x u_y^2 u_z^2 + 2u_y u_z^2 \widetilde{\Pi}_{xy} + 2u_y^2 u_z \widetilde{\Pi}_{xz} + 4u_x u_y u_z \widetilde{\Pi}_{yz} + \left(u_x u_y^2 + u_x u_z^2 \right) \widetilde{T}/3 \right.$$
$$+ \left(-u_x u_y^2 - u_x u_z^2 \right) \widetilde{N}_{xz}/3 + \left(-u_x u_y^2 + 2u_x u_z^2 \right) \widetilde{N}_{yz}/3 + 4u_y u_z \widetilde{Q}_{xyz} + u_z^2 \widetilde{Q}_{xyy} + u_y^2 \widetilde{Q}_{xzz}$$
$$\left. + 2u_x u_y \widetilde{Q}_{yzz} + 2u_x u_z \widetilde{Q}_{yyz} + 2u_y \widetilde{M}_{112} + 2u_z \widetilde{M}_{121} + u_x \widetilde{M}_{022} \right],$$

(A20)

$$\widetilde{M}_{212} = M_{212} - \left[u_x^2 u_y u_z^2 + 2u_x u_z^2 \widetilde{\Pi}_{xy} + 4u_x u_y u_z \widetilde{\Pi}_{xz} + 2u_x^2 u_z \widetilde{\Pi}_{yz} + \left(u_x^2 u_y + u_y u_z^2 \right) \widetilde{T}/3 \right.$$
$$+ \left(-u_x^2 u_y + 2u_y u_z^2 \right) \widetilde{N}_{xz}/3 + \left(-u_x^2 u_y - u_y u_z^2 \right) \widetilde{N}_{yz}/3 + 4u_x u_z \widetilde{Q}_{xyz} + 2u_x u_y \widetilde{Q}_{xzz} + u_z^2 \widetilde{Q}_{xxy}$$
$$\left. + u_x^2 \widetilde{Q}_{yzz} + 2u_y u_z \widetilde{Q}_{xxz} + 2u_z \widetilde{M}_{211} + 2u_x \widetilde{M}_{112} + u_y \widetilde{M}_{202} \right)$$

(A21)

$$\widetilde{M}_{221} = M_{221} - \left(u_x^2 u_y^2 u_z + 4u_x u_y u_z \widetilde{\Pi}_{xy} + 2u_x u_y^2 \widetilde{\Pi}_{xz} + 2u_x^2 u_y \widetilde{\Pi}_{yz} + \left(u_x^2 u_z + u_y^2 u_z \right) \widetilde{T}/3 \right.$$
$$+ \left(-u_x^2 u_z + 2u_y^2 u_z \right) \widetilde{N}_{xz}/3 + \left(2u_x^2 u_z - u_y^2 u_z \right) \widetilde{N}_{yz}/3 + 4u_x u_y \widetilde{Q}_{xyz} + 2u_x u_z \widetilde{Q}_{xyy}$$
$$\left. + 2u_y u_z \widetilde{Q}_{xxy} + u_y^2 \widetilde{Q}_{xxz} + u_x^2 \widetilde{Q}_{yyz} + 2u_y \widetilde{M}_{211} + 2u_x \widetilde{M}_{121} + u_z \widetilde{M}_{220} \right],$$

(A22)

$$\widetilde{M}_{222} = M_{222} - \left[u_x^2 u_y^2 u_z^2 + 4u_x u_y u_z^2 \widetilde{\Pi}_{xy} + 4u_x u_y^2 u_z \widetilde{\Pi}_{xz} + 4u_x^2 u_y u_z \widetilde{\Pi}_{yz} + \left(u_x^2 u_y^2 + u_x^2 u_z^2 + u_y^2 u_z^2 \right) \widetilde{T}/3 \right.$$
$$+ \left(-u_x^2 u_y^2 - u_x^2 u_z^2 + 2u_y^2 u_z^2 \right) \widetilde{N}_{xz}/3 + \left(-u_x^2 u_y^2 + 2u_x^2 u_z^2 - u_y^2 u_z^2 \right) \widetilde{N}_{yz}/3 + 8u_x u_y u_z \widetilde{Q}_{xyz} + 2u_x u_z^2 \widetilde{Q}_{xyy} + 2u_x u_y^2 \widetilde{Q}_{xzz}$$
$$+ 2u_y u_z^2 \widetilde{Q}_{xxy} + 2u_x^2 u_y \widetilde{Q}_{yzz} + 2u_y^2 u_z \widetilde{Q}_{xxz} + 2u_x^2 u_z \widetilde{Q}_{yyz} + u_x^2 \widetilde{M}_{022} + u_y^2 \widetilde{M}_{202} + u_z^2 \widetilde{M}_{220} + 4u_y u_z \widetilde{M}_{211}$$
$$\left. + 4u_x u_z \widetilde{M}_{121} + 4u_x u_y \widetilde{M}_{112} + 2u_x \widetilde{M}_{122} + 2u_y \widetilde{M}_{212} + 2u_z \widetilde{M}_{221} \right].$$

(A23)

Substituting Eqs. (A1)–(A23) into Eq. (21), one arrives at the moment representation in the central basis:

$$f_{(0,0,0)} = \rho \left\{ - \left(u_x^2 - 1 \right) \left(u_y^2 - 1 \right) \left(u_z^2 - 1 \right) - 4u_x u_y \left(u_z^2 - 1 \right) \widetilde{\Pi}_{xy} - 4u_x u_z \left(u_y^2 - 1 \right) \widetilde{\Pi}_{xz} - 4u_y u_z \left(u_x^2 - 1 \right) \widetilde{\Pi}_{yz} \right.$$
$$+ \left[u_x^2 \left(u_y^2 + u_z^2 - 2 \right) + u_z^2 \left(1 - 2u_y^2 \right) + u_y^2 \right] \widetilde{N}_{xz}/3 + \left[u_y^2 \left(u_x^2 + u_z^2 - 2 \right) + u_z^2 \left(1 - 2u_x^2 \right) + u_x^2 \right] \widetilde{N}_{yz}/3$$
$$- \left[u_x^2 u_y^2 + u_x^2 u_z^2 + u_y^2 u_z^2 - 2 \left(u_x^2 + u_y^2 + u_z^2 \right) + 3 \right] \widetilde{T}/3 - 8u_x u_y u_z \widetilde{Q}_{xyz} - 2u_x \left(u_z^2 - 1 \right) \widetilde{Q}_{xyy} - 2u_x \left(u_y^2 - 1 \right) \widetilde{Q}_{xzz}$$
$$- 2u_y \left(u_z^2 - 1 \right) \widetilde{Q}_{xxy} - 2u_y \left(u_x^2 - 1 \right) \widetilde{Q}_{yzz} - 2u_z \left(u_y^2 - 1 \right) \widetilde{Q}_{xxz} - 2u_z \left(u_x^2 - 1 \right) \widetilde{Q}_{yyz} + \left(1 - u_x^2 \right) \widetilde{M}_{022} + \left(1 - u_y^2 \right) \widetilde{M}_{202}$$
$$\left. + \left(1 - u_z^2 \right) \widetilde{M}_{220} - 4u_y u_z \widetilde{M}_{211} - 4u_x u_z \widetilde{M}_{121} - 4u_x u_y \widetilde{M}_{112} - 2u_x \widetilde{M}_{122} - 2u_y \widetilde{M}_{212} - 2u_z \widetilde{M}_{221} - \widetilde{M}_{222} \right\},$$

(A24)

$$f_{(\sigma,0,0)} = \tfrac{1}{6} \rho \left(3u_x \left(u_y^2 - 1 \right) \left(u_z^2 - 1 \right) (\sigma + u_x) + 6u_y \left(u_z^2 - 1 \right) (\sigma + 2u_x) \widetilde{\Pi}_{xy} + 6u_z \left(u_y^2 - 1 \right) (\sigma + 2u_x) \widetilde{\Pi}_{xz} \right.$$
$$+ 12u_x u_y u_z (\sigma + u_x) \widetilde{\Pi}_{yz} - \left[\sigma u_x \left(u_y^2 + u_z^2 - 2 \right) + u_x^2 \left(u_y^2 + u_z^2 - 2 \right) - 2 \left(u_y^2 - 1 \right) \left(u_z^2 - 1 \right) \right] \widetilde{N}_{xz}$$
$$+ \left\{ u_z^2 \left[2u_x (\sigma + u_x) - u_y^2 \right] - u_x \left(u_y^2 + 1 \right) (\sigma + u_x) + u_y^2 + u_z^2 - 1 \right\} \widetilde{N}_{yz} + \left\{ u_z^2 \left[u_x (\sigma + u_x) + u_y^2 \right] + u_x \left(u_y^2 - 2 \right) (\sigma + u_x) \right.$$
$$\left. - u_y^2 - u_z^2 + 1 \right\} \widetilde{T} + 12u_y u_z (\sigma + 2u_x) \widetilde{Q}_{xyz} + 3 \left(u_z^2 - 1 \right) (\sigma + 2u_x) \widetilde{Q}_{xyy} + 3 \left(u_y^2 - 1 \right) (\sigma + 2u_x) \widetilde{Q}_{xzz}$$
$$+ 6u_y \left(u_z^2 - 1 \right) \widetilde{Q}_{xxy} + 6u_x u_y (\sigma + u_x) \widetilde{Q}_{yzz} + 6u_z \left(u_y^2 - 1 \right) \widetilde{Q}_{xxz} + 6u_x u_z (\sigma + u_x) \widetilde{Q}_{yyz} + 3u_x (\sigma + u_x) \widetilde{M}_{022}$$

$$+ 3(u_y^2 - 1)\widetilde{M}_{202} + 3(u_z^2 - 1)\widetilde{M}_{220} + 12u_y u_z \widetilde{M}_{211} + 6u_z(\sigma + 2u_x)\widetilde{M}_{121} + 6u_y(\sigma + 2u_x)\widetilde{M}_{112}$$
$$+ 3(\sigma + 2u_x)\widetilde{M}_{122} + 6u_y \widetilde{M}_{212} + 6u_z \widetilde{M}_{221} + 3\widetilde{M}_{222}\big), \tag{A25}$$

$$f_{(0,\lambda,0)} = \tfrac{1}{6}\rho\big(3u_y(u_x^2 - 1)(u_z^2 - 1)(\lambda + u_y) + 6u_x(u_z^2 - 1)(\lambda + 2u_y)\widetilde{\Pi}_{xy} + 12u_x u_y u_z(\lambda + u_y)\widetilde{\Pi}_{xz} + 6u_z(u_x^2 - 1)(\lambda + 2u_y)\widetilde{\Pi}_{yz}$$
$$+ \big(-u_x^2[u_y(\lambda + u_y) + u_z^2 - 1] + u_y(2u_z^2 - 1)(\lambda + u_y) + u_z^2 - 1\big\}\widetilde{N}_{xz} + \big\{-u_x^2[u_y(\lambda + u_y) - 2u_z^2 + 2]$$
$$- u_y(u_z^2 - 2)(\lambda + u_y) - 2u_z^2 + 2\big\}\widetilde{N}_{yz} + \big\{u_x^2[u_y(\lambda + u_y) + u_z^2 - 1] + u_y(u_z^2 - 2)(\lambda + u_y) - u_z^2 + 1\big\}\widetilde{T}$$
$$+ 12u_x u_z(\lambda + 2u_y)\widetilde{Q}_{xyz} + 6u_x(u_z^2 - 1)\widetilde{Q}_{xyy} + 6u_x u_y(\lambda + u_y)\widetilde{Q}_{xzz} + 3(u_z^2 - 1)(\lambda + 2u_y)\widetilde{Q}_{xxy} + 3(u_x^2 - 1)(\lambda + 2u_y)\widetilde{Q}_{yzz}$$
$$+ 6u_y u_z(\lambda + u_y)\widetilde{Q}_{xxz} + 6u_z(u_x^2 - 1)\widetilde{Q}_{yyz} + 3(u_x^2 - 1)\widetilde{M}_{022} + 3u_y(\lambda + u_y)\widetilde{M}_{202} + 3(u_z^2 - 1)\widetilde{M}_{220}$$
$$+ 6u_z(\lambda + 2u_y)\widetilde{M}_{211} + 12u_x u_z \widetilde{M}_{121} + 6u_x(\lambda + 2u_y)\widetilde{M}_{112} + 6u_x \widetilde{M}_{122} + 3(\lambda + 2u_y)\widetilde{M}_{212} + 6u_z \widetilde{M}_{221} + 3\widetilde{M}_{222}\big), \tag{A26}$$

$$f_{(0,0,\delta)} = \tfrac{1}{6}\rho\big(3u_z(u_x^2 - 1)(u_y^2 - 1)(\delta + u_z) + 12u_x u_y u_z(\delta + u_z)\widetilde{\Pi}_{xy} + 6u_x(u_y^2 - 1)(\delta + 2u_z)\widetilde{\Pi}_{xz} + 6u_y(u_x^2 - 1)(\delta + 2u_z)\widetilde{\Pi}_{yz}$$
$$+ \big\{-u_x^2[u_z(\delta + u_z) + u_y^2 - 1] + u_y^2[2u_z(\delta + u_z) + 1] - u_z(\delta + u_z) - 1\big\}\widetilde{N}_{xz} + \big\{u_x^2[2u_z(\delta + u_z) - u_y^2 + 1]$$
$$- u_y^2[u_z(\delta + u_z) - 1] - u_z(\delta + u_z) - 1\big\}\widetilde{N}_{yz} + \big\{u_x^2[u_z(\delta + u_z) + u_y^2 - 1] + u_y^2[u_z(\delta + u_z) - 1] - 2u_z(\delta + u_z) + 1\big\}\widetilde{T}$$
$$+ 12u_x u_y(\delta + 2u_z)\widetilde{Q}_{xyz} + 6u_x u_z(\delta + u_z)\widetilde{Q}_{xyy} + 6u_x(u_y^2 - 1)\widetilde{Q}_{xzz} + 6u_y u_z(\delta + u_z)\widetilde{Q}_{xxy} + 6u_y(u_x^2 - 1)\widetilde{Q}_{yzz}$$
$$+ 3(u_y^2 - 1)(\delta + 2u_z)\widetilde{Q}_{xxz} + 3(u_x^2 - 1)(\delta + 2u_z)\widetilde{Q}_{yyz} + 3(u_x^2 - 1)\widetilde{M}_{022} + 3(u_y^2 - 1)\widetilde{M}_{202} + 3u_z(\delta + u_z)\widetilde{M}_{220}$$
$$+ 6u_y(\delta + 2u_z)\widetilde{M}_{211} + 6u_x(\delta + 2u_z)\widetilde{M}_{121} + 12u_x u_y \widetilde{M}_{112} + 6u_x \widetilde{M}_{122} + 6u_y \widetilde{M}_{212} + 3(\delta + 2u_z)\widetilde{M}_{221} + 3\widetilde{M}_{222}\big), \tag{A27}$$

$$f_{(\sigma,\lambda,0)} = \tfrac{1}{4}\rho\big(-u_x u_y(u_z^2 - 1)(\lambda + u_y)(\sigma + u_x) - (u_z^2 - 1)(\lambda + 2u_y)(\sigma + 2u_x)\widetilde{\Pi}_{xy} - 2u_y u_z(\lambda + u_y)(\sigma + 2u_x)\widetilde{\Pi}_{xz}$$
$$- u_x u_z(\lambda + 2u_y)(\sigma + u_x)\widetilde{\Pi}_{yz} + \tfrac{1}{3}\big\{\sigma u_x[u_y(\lambda + u_y) + u_z^2 - 1] + u_x^2[u_y(\lambda + u_y) + u_z^2 - 1] - 2u_y(u_z^2 - 1)(\lambda + u_y)\big\}\widetilde{N}_{xz}$$
$$+ \tfrac{1}{3}\big\{\sigma u_x[u_y(\lambda + u_y) - 2u_z^2 + 2] + u_x^2[u_y(\lambda + u_y) - 2u_z^2 + 2] + u_y(u_z^2 - 1)(\lambda + u_y)\big\}\widetilde{N}_{yz}$$
$$+ \tfrac{1}{3}\big\{-\sigma u_x[u_y(\lambda + u_y) + u_z^2 - 1] - u_x^2[u_y(\lambda + u_y) + u_z^2 - 1] - u_y(u_z^2 - 1)(\lambda + u_y)]\widetilde{T} - 2u_z(\lambda + 2u_y)(\sigma + 2u_x)\widetilde{Q}_{xyz}$$
$$- (u_z^2 - 1)(\sigma + 2u_x)\widetilde{Q}_{xyy} - u_y(\lambda + u_y)(\sigma + 2u_x)\widetilde{Q}_{xzz} - (u_z^2 - 1)(\lambda + 2u_y)\widetilde{Q}_{xxy} - u_x(\lambda + 2u_y)(\sigma + u_x)\widetilde{Q}_{yzz}$$
$$- 2u_y u_z(\lambda + u_y)\widetilde{Q}_{xxz} - 2u_x u_z(\sigma + u_x)\widetilde{Q}_{yyz} - u_x(\sigma + u_x)\widetilde{M}_{022} - u_y(\lambda + u_y)\widetilde{M}_{202} + (1 - u_z^2)\widetilde{M}_{220}$$
$$- 2u_z(\lambda + 2u_y)\widetilde{M}_{211} - 2u_z(\sigma + 2u_x)\widetilde{M}_{121} - (\lambda + 2u_y)(\sigma + 2u_x)\widetilde{M}_{112}$$
$$- (\sigma + 2u_x)\widetilde{M}_{122} - (\lambda + 2u_y)\widetilde{M}_{212} - 2u_z \widetilde{M}_{221} - \widetilde{M}_{222}\big), \tag{A28}$$

$$f_{(\sigma,0,\delta)} = \tfrac{1}{4}\rho\big(-u_x u_z(u_y^2 - 1)(\delta + u_z)(\sigma + u_x) - 2u_y u_z(\delta + u_z)(\sigma + 2u_x)\widetilde{\Pi}_{xy} - (u_y^2 - 1)(\delta + 2u_z)(\sigma + 2u_x)\widetilde{\Pi}_{xz}$$
$$- 2u_x u_y(\delta + 2u_z)(\sigma + u_x)\widetilde{\Pi}_{yz} + \tfrac{1}{3}\big\{\sigma u_x[u_z(\delta + u_z) + u_y^2 - 1] + u_x^2[u_z(\delta + u_z) + u_y^2 - 1] - 2(u_y^2 - 1)u_z(\delta + u_z)\big\}\widetilde{N}_{xz}$$
$$+ \tfrac{1}{3}\big\{\sigma u_x[-2u_z(\delta + u_z) + u_y^2 - 1] + u_x^2[-2u_z(\delta + u_z) + u_y^2 - 1] + (u_y^2 - 1)u_z(\delta + u_z)\big\}\widetilde{N}_{yz}$$
$$+ \tfrac{1}{3}\big\{-\sigma u_x[u_z(\delta + u_z) + u_y^2 - 1] - u_x^2[u_z(\delta + u_z) + u_y^2 - 1] - (u_y^2 - 1)u_z(\delta + u_z)\big\}\widetilde{T} - 2u_y(\delta + 2u_z)(\sigma + 2u_x)\widetilde{Q}_{xyz}$$
$$- u_z(\delta + u_z)(\sigma + 2u_x)\widetilde{Q}_{xyy} - (u_y^2 - 1)(\sigma + 2u_x)\widetilde{Q}_{xzz} - 2u_y u_z(\delta + u_z)\widetilde{Q}_{xxy} - 2u_x u_y(\sigma + u_x)\widetilde{Q}_{yzz}$$
$$- (u_y^2 - 1)(\delta + 2u_z)\widetilde{Q}_{xxz} - u_x(\delta + 2u_z)(\sigma + u_x)\widetilde{Q}_{yyz} - u_x(\sigma + u_x)\widetilde{M}_{022} + (1 - u_y^2)\widetilde{M}_{202} - u_z(\delta + u_z)\widetilde{M}_{220}$$
$$- 2u_y(\delta + 2u_z)\widetilde{M}_{211} - (\delta + 2u_z)(\sigma + 2u_x)\widetilde{M}_{121} - 2u_y(\sigma + 2u_x)\widetilde{M}_{112}$$
$$- (\sigma + 2u_x)\widetilde{M}_{122} - 2u_y \widetilde{M}_{212} - (\delta + 2u_z)\widetilde{M}_{221} - \widetilde{M}_{222}\big), \tag{A29}$$

$$f_{(0,\lambda,\delta)} = \tfrac{1}{4}\rho\big(-u_y u_z(u_x^2 - 1)(\delta + u_z)(\lambda + u_y) - 2u_x u_z(\delta + u_z)(\lambda + 2u_y)\widetilde{\Pi}_{xy} - 2u_x u_y(\delta + u_z)(\lambda + u_y)\widetilde{\Pi}_{xz}$$
$$- (u_x^2 - 1)(\delta + 2u_z)(\lambda + 2u_y)\widetilde{\Pi}_{yz} + \tfrac{1}{3}\big\{\lambda u_y[-2u_z(\delta + u_z) + u_x^2 - 1] + u_y^2[-2u_z(\delta + u_z) + u_x^2 - 1]$$
$$+ (u_x^2 - 1)u_z(\delta + u_z)\big\}\widetilde{N}_{xz} + \tfrac{1}{3}\big\{\lambda u_y[u_z(\delta + u_z) + u_x^2 - 1] + u_y^2[u_z(\delta + u_z) + u_x^2 - 1] - 2(u_x^2 - 1)u_z(\delta + u_z)\big\}\widetilde{N}_{yz}$$
$$+ \tfrac{1}{3}\big\{-\lambda u_y[u_z(\delta + u_z) + u_x^2 - 1] - u_y^2[u_z(\delta + u_z) + u_x^2 - 1] - (u_x^2 - 1)u_z(\delta + u_z)\big\}\widetilde{T} - 2u_x(\delta + 2u_z)(\lambda + 2u_y)\widetilde{Q}_{xyz}$$

$$
\begin{aligned}
&-2u_x u_z(\delta + u_z)\widetilde{Q}_{xyy} - 2u_x u_y(\lambda + u_y)\widetilde{Q}_{xzz} - u_z(\delta + u_z)(\lambda + 2u_y)\widetilde{Q}_{xxy} - (u_x^2 - 1)(\lambda + 2u_y)\widetilde{Q}_{yzz} \\
&- u_y(\delta + 2u_z)(\lambda + u_y)\widetilde{Q}_{xxz} - (u_x^2 - 1)(\delta + 2u_z)\widetilde{Q}_{yyz} + (1 - u_x^2)\widetilde{M}_{022} - u_y(\lambda + u_y)\widetilde{M}_{202} - u_z(\delta + u_z)\widetilde{M}_{220} - (\delta + 2u_z) \\
&\times (\lambda + 2u_y)\widetilde{M}_{211} - 2u_x(\delta + 2u_z)\widetilde{M}_{121} - 2u_x(\lambda + 2u_y)\widetilde{M}_{112} - 2u_x\widetilde{M}_{122} - (\lambda + 2u_y)\widetilde{M}_{212} - (\delta + 2u_z)\widetilde{M}_{221} - \widetilde{M}_{222}),
\end{aligned}
\tag{A30}
$$

$$
\begin{aligned}
f_{(\sigma,\lambda,\delta)} = \tfrac{1}{8}\rho\big(&u_x u_y u_z(\delta + u_z)(\lambda + u_y)(\sigma + u_x) + u_z(\delta + u_z)(\lambda + 2u_y)(\sigma + 2u_x)\widetilde{\Pi}_{xy} + u_y(\delta + 2u_z)(\lambda + u_y)(\sigma + 2u_x)\widetilde{\Pi}_{xz} \\
&+ u_x(\delta + 2u_z)(\lambda + 2u_y)(\sigma + u_x)\widetilde{\Pi}_{yz} + \tfrac{1}{3}\big\{ -\delta u_z[u_x(\sigma + u_x) - 2u_y(\lambda + u_y)] - u_z^2[u_x(\sigma + u_x) - 2u_y(\lambda + u_y)] \\
&- u_x u_y(\lambda + u_y)(\sigma + u_x)\big\}\widetilde{N}_{xz} + \tfrac{1}{3}\big\{\delta u_z[2u_x(\sigma + u_x) - u_y(\lambda + u_y)] + u_z^2[2u_x(\sigma + u_x) - u_y(\lambda + u_y)] \\
&- u_x u_y(\lambda + u_y)(\sigma + u_x)\big\}\widetilde{N}_{yz} + \tfrac{1}{3}\big\{\delta u_z[u_y(\lambda + u_y) + u_x(\sigma + u_x)] + u_z^2[u_y(\lambda + u_y) + u_x(\sigma + u_x)] \\
&+ u_x u_y(\lambda + u_y)(\sigma + u_x)\big\}\widetilde{T} + (\delta + 2u_z)(\lambda + 2u_y)(\sigma + 2u_x)\widetilde{Q}_{xyz} + u_z(\delta + u_z)(\sigma + 2u_x)\widetilde{Q}_{xyy} \\
&+ u_y(\lambda + u_y)(\sigma + 2u_x)\widetilde{Q}_{xzz} + u_z(\delta + u_z)(\lambda + 2u_y)\widetilde{Q}_{xxy} + u_x(\lambda + 2u_y)(\sigma + u_x)\widetilde{Q}_{yzz} + u_y(\delta + 2u_z)(\lambda + u_y)\widetilde{Q}_{xxz} \\
&+ u_x(\delta + 2u_z)(\sigma + u_x)\widetilde{Q}_{yyz} + u_x(\sigma + u_x)\widetilde{M}_{022} + u_y(\lambda + u_y)\widetilde{M}_{202} + u_z(\delta + u_z)\widetilde{M}_{220} + (\delta + 2u_z)(\lambda + 2u_y)\widetilde{M}_{211} \\
&+ (\delta + 2u_z)(\sigma + 2u_x)\widetilde{M}_{121} + (\lambda + 2u_y)(\sigma + 2u_x)\widetilde{M}_{112} + (\sigma + 2u_x)\widetilde{M}_{122} + (\lambda + 2u_y)\widetilde{M}_{212} + (\delta + 2u_z)\widetilde{M}_{221} + \widetilde{M}_{222}\big),
\end{aligned}
\tag{A31}
$$

[1] R. Benzi, S. Succi, and M. Vergassola, Phys. Rep. **222**, 145 (1992).

[2] S. Succi, *The Lattice Boltzmann Equation for Fluid Dynamics and Beyond* (Oxford University Press, Oxford, 2001).

[3] H. Chen, S. Kandasamy, S. Orszag, R. Shock, S. Succi, and V. Yakhot, Science **301**, 633 (2003).

[4] S. Ansumali, I. V. Karlin, S. Arcidiacono, A. Abbas, and N. I. Prasianakis, Phys. Rev. Lett. **98**, 124502 (2007).

[5] M. R. Swift, W. R. Osborn, and J. M. Yeomans, Phys. Rev. Lett. **75**, 830 (1995).

[6] A. Mazloomi M, S. S. Chikatamarla, and I. V. Karlin, Phys. Rev. Lett. **114**, 174502 (2015).

[7] M. Mendoza, B. M. Boghosian, H. J. Herrmann, and S. Succi, Phys. Rev. Lett. **105**, 014502 (2010).

[8] R. Benzi, S. Chibbaro, and S. Succi, Phys. Rev. Lett. **102**, 026002 (2009).

[9] H. Chen, S. Chen, and W. H. Matthaeus, Phys. Rev. A **45**, R5339 (1992).

[10] Y. H. Qian, D. dHumieres, and P. Lallemand, Europhys. Lett. **17**, 479 (1992).

[11] I. V. Karlin, A. Ferrante, and H. C. Öttinger, Europhys. Lett. **47**, 182 (1999).

[12] S. Ansumali, I. V. Karlin, and H. C. Öttinger, Europhys. Lett. **63**, 798 (2003).

[13] F. Bösch and I. V. Karlin, Phys. Rev. Lett. **111**, 090601 (2013).

[14] C. K. Aidun and J. R. Clausen, Annu. Rev. Fluid. Mech. **42**, 439 (2010).

[15] S. S. Chikatamarla and I. V. Karlin, Physica A **392**, 1925 (2013).

[16] S. S. Chikatamarla, S. Ansumali, and I. V. Karlin, Phys. Rev. Lett. **97**, 010201 (2006).

[17] P. J. Dellar, J. Comput. Phys. **190**, 351 (2003).

[18] F. Higuera, S. Succi, and R. Benzi, Europhys. Lett. **9**, 345 (1989).

[19] D. d'Humières, AIAA Prog. Aeronaut. Astronaut. **159**, 450 (1992).

[20] P. Lallemand and L.-S. Luo, Phys. Rev. E **61**, 6546 (2000).

[21] M. Geier, A. Greiner, and J. G. Korvink, Phys. Rev. E **73**, 066705 (2006).

[22] H. Chen, R. Zhang, I. Staroselsky, and M. Jhon, Physica A **362**, 125 (2006).

[23] J. Latt and B. Chopard, Math. Comput. Simul. **72**, 165 (2006).

[24] R. K. Freitas, A. Henze, M. Meinke, and W. Schroeder, Comput. Fluids **47**, 115 (2011).

[25] I. V. Karlin, F. Bösch, and S. S. Chikatamarla, Phys. Rev. E **90**, 031302(R) (2014).

[26] S. G. Johnson, "Notes on fft-based differentiation", http://math.mit.edu/~stevenj/fft-deriv.pdf (2011).

[27] R. Mei, L.-S. Luo, P. Lallemand, and D. d'Humières, Comput. Fluids **35**, 855 (2006).

[28] S. Kida, J. Phys. Soc. Jpn. **54**, 2132 (1985).

[29] S. Kida and Y. Murakami, Phys. Fluids (1958–1988) **30**, 2030 (1987).

[30] B. Keating, G. Vahala, J. Yepez, M. Soe, and L. Vahala, Phys. Rev. E **75**, 036712 (2007).

[31] S. S. Chikatamarla, C. E. Frouzakis, I. V. Karlin, A. G. Tomboulides, and K. B. Boulouchos, J. Fluid Mech. **656**, 298 (2010).

[32] A. N. Kolmogorov, Dokl. Akad. Nauk SSSR **30**, 301 (1941).

[33] A. N. Kolmogorov, Dokl. Akad. Nauk SSSR **32**, 16 (1941).

[34] F. Bösch, S. S. Chikatamarla, and I. V. Karlin, arXiv:1507.02509 [physics.flu-dyn] (2015).

[35] G. K. Batchelor, *An Introduction to Fluid Dynamics* (Cambridge University Press, Cambridge, 2000).

[36] H. Lamb, *Hydrodynamics* (Cambridge University Press, Cambridge, 1932).